(Re)submitted to The Astrophysical Journal 10/04/02.

On the Spiral Structure of NGC 2915 and Dark Matter

F. S. Masset[1]

Service d'Astrophysique, CE-Saclay, 91191 Gif/Yvette Cedex, France

fmasset@cea.fr

and

M. Bureau[2]

Columbia Astrophysics Laboratory, 550 West 120th Street, 1027 Pupin Hall, MC 5247, New York, NY 10027

bureau@astro.columbia.edu

ABSTRACT

NGC 2915 is a blue compact dwarf galaxy embedded in an extended, low surface brightness H I disk exhibiting a two-armed spiral structure and a central bar-like component. Commonly accepted mechanisms are unable to explain the existence of these patterns and Bureau et al. proposed disk dark matter (scaling with the H I distribution) or a rotating triaxial dark halo as alternative solutions. In an attempt to explore these mechanisms, hydrodynamical simulations were run for each case and compared to observations using customized column density and kinematic constraints. The spiral structure can be accounted for both by an unseen bar or triaxial halo, the former fitting the observations slightly better. However, the large bar mass or halo pattern frequency required make it unlikely that the spiral wave is driven by an external perturber. In particular, the spin parameter λ is much higher than predicted by current cold dark matter (CDM) structure formation scenarios. The massive disk models show that when the observed gas surface density is scaled up by a factor about 10, the disk develops a spiral structure resembling closely the observed one, in perturbed density as well as perturbed velocity. This is consistent with more limited studies in other galaxies and suggests that the disk of NGC 2915 contains much more mass than is visible, tightly linked to the neutral hydrogen. A classic (quasi-)spherical halo is nevertheless still required, as increasing the disk mass further to fit the circular velocity curve would make

---

[1]Send offprint requests to F. S. Masset: fmasset@cea.fr

[2]Hubble Fellow

the disk violently unstable. Scaling the observed surface density profile by an order of magnitude brings the disk and halo masses to comparable values within the disk radius. The surface density remains under Kennicutt's star formation threshold for a gaseous disk and no stars are expected to form, as required by observations.

Subject headings: dark matter — galaxies: evolution — galaxies: halos — galaxies: individual (NGC 2915) — galaxies: kinematics and dynamics — ISM: kinematics and dynamics

1. Introduction

NGC 2915 is a blue compact dwarf (BCD) galaxy at a distance $D = 5.3 \pm 1.6$ Mpc (Meurer, Mackie, & Carignan 1994). In the optical, it displays a high surface brightness blue core and a red diffuse population. The core is the locus of high mass star formation and possesses a high excitation, low metallicity H II region spectrum; the red population has an exponential profile with a low extrapolated central surface brightness (Meurer et al. 1994). The radio properties of NGC 2915 are rather extreme, with an H I disk extending to 22 radial scalelengths in the B-band (5 Holmberg radii; Meurer et al. 1996). This disk displays a short central bar overlapping the optical emission and a well-developed outer two-armed spiral extending to its edge (see Fig. 1). The signature of an oval distortion is also present in the velocity field. Standard modeling of the derived circular velocity curve yields a blue mass-to-light ratio $\mathcal{M}_T/L_B \gtrsim 65$ at the last measured point ($\mathcal{M}_{\rm dark}/\mathcal{M}_{\rm luminous} \approx 19$), making NGC 2915 one of the darkest disk galaxies known (Meurer et al. 1996). The core of the dark matter halo also appears unusually dense and compact. In fact, the stellar content can be neglected at all radii without greatly affecting the fit. The optical properties of NGC 2915, discussed in more detail by Meurer et al. (1994), are thus unimportant for this work. We will rather focus on its unique H I properties, described more fully in Meurer et al. (1996).

Bureau et al. (1999) discussed the origin of the H I bar and spiral pattern in NGC 2915. They argue for a common, slow pattern speed $\Omega_p = 8.0 \pm 2.4$ km s^{-1} kpc^{-1}, yielding a corotation radius to bar semi-length ratio $r_{\rm cr}/r_b \gtrsim 1.7$ ($r_b = 180'' = 4.6$ kpc). This lower limit is reached for $\Omega_p = 10.4$ km s^{-1} kpc^{-1}, while the limited extent of the circular velocity curve prevents the derivation of a proper upper limit. Although Bureau et al.'s (1999) measurement using Tremaine & Weinberg (1984a) method is plagued by uncertainties, it is consistent with the idea that bars in dense halos should be slow (e.g. Debattista & Sellwood 1998). Furthermore, the low (luminous) disk surface density and the locations of the pseudo-rings make it unlikely that swing amplification (Toomre 1981) or bar-driving (Schwarz 1981, 1984; Byrd et al. 1994) can explain the bar and spiral patterns. Because NGC 2915 is isolated, gravitational interactions cannot be invoked as an exciting mechanism either (Noguchi 1987). Bureau et al. (1999) proposed two alternatives: i) the H I disk is embedded in a massive and extended triaxial dark halo with a rotating figure, forcing the bar and spiral pattern at a certain frequency, or ii) (some) dark matter is distributed in a disk closely following the H I distribution, rendering the disk gravitationally unstable. Although both solutions lack direct observational support (but see Pfenniger, Combes, & Martinet 1994 for the latter), they offer a way forward.

The purpose of this paper is to investigate whether either (or both) of these mechanisms works in practice. The rotating halo shall be modeled by external forcing from a rotating triaxial potential (which could be due to a rotating triaxial halo, bulge, central bar, or a mixture of those), and the massive disk will be modeled by simply scaling up the gaseous surface density of the disk. We test the models by running a simple two-dimensional (hereafter 2D) hydrodynamic code, exploring the available parameter space, and comparing with the observations. In § 2, we first present the relevant parameters for both sets of models and describe suitable observational constraints. A brief description of the code is provided in § 3. The results for the external perturber models are presented and discussed in § 4, while those for the massive disk models are described in § 5. We summarize all results and conclude briefly in § 6.

2. Disk Response to a Rotating Non-Axisymmetric Forcing Potential

Fig. 1 shows the total H I map and velocity field of NGC 2915 from the naturally-weighted cube of Meurer et al. (1996), which we will use here for comparison purposes. The high surface brightness core of NGC 2915 (blue and lumpy) is entirely contained within one beam width. Azimuthal averages of the gaseous surface density $\Sigma_g \equiv 4/3\,\Sigma_{HI}$, the circular velocity v_c, and the H I velocity dispersion σ_v are presented in Fig. 2 (see Meurer et al. 1996; Bureau et al. 1999). These profiles are based on higher spatial resolution uniformly-weighted data for $r \lesssim 10$ kpc and naturally-weighted data at larger radii. The H I has a central peak but decreases slowly in the outer parts. The circular velocity rises within $r \approx 5$ kpc and levels out at $v_c \approx 80$ km s^{-1} at larger radii. The velocity dispersion is the usual $8-10$ km s^{-1} outside 5 kpc but is much higher in the central regions, justifying the use of an asymmetric drift correction to the rotation curve by Meurer et al. (1996). We note however that the velocity dispersion in the central regions may be overestimated due to beam smearing effects (although Meurer et al. 1996 argue against this), and that in turn the circular velocity may be over-corrected (i.e. overestimated) within $r \lesssim 3$ kpc. The Toomre Q parameter (Toomre 1964) estimated from this data is high everywhere ($Q \gtrsim 6$; see Bureau et al. 1999), implying that gravitational instabilities such as SWING (Toomre 1981) can not grow if one assumes that the observed gas surface density accounts for the entire disk mass. As mentioned above, to force the emergence of spiral arms, one can then study the response of the disk to an external forcing potential or artificially increase the disk mass.

To fit the models to the observations, one needs to identify the relevant constraints provided by the data and the parameters one can adjust to improve the match. The basic constraints are provided by the first three moments of the data cube, shown in Fig. 1–2, but we refine these below.

2.1. Constraints from the Column Density Map

Although the disk response in NGC 2915 is likely non-linear, it is instructive to look at the dispersion relation for an m-folded density wave in a thin isothermal disk of sound speed c_s, in the WKB limit (Lin & Shu 1964):

$$m^2(\Omega - \Omega_p)^2 = \kappa^2 - 2\pi G\Sigma_g|k| + k^2 c_s^2, \tag{1}$$

where $k^2 = m^2/r^2 + k_r^2$, k_r is the radial wave vector, Ω_p is the pattern frequency of the bar and spiral arms (i.e. the pattern frequency of the forcing potential), Ω is the orbital frequency (v_c/r), and κ is the epicyclic frequency. We shall neglect hereafter the possibility that the spiral arms have a different (slower) pattern speed than the bar, see e.g. Masset & Tagger (1997) and references therein. Inspection of the amplitude spectra (or periodograms) of the $m = 2$ perturbations which appear in our runs shows that this assumption is reasonable. More precisely, one could think of a halo with a slow figure rotation, the ILR of which would coincide with the disk spiral corotation. We have performed early runs with halo pattern speeds down to $\Omega_p = 3$ km s^{-1} kpc^{-1}, and the power spectra of the disk response show no trace at all of any response at any other frequency than Ω_p. This is not entirely a surprise however: on the contrary to what happens for a massive collisionless disk, the spiral density waves propagate *inwards* from the ILR and *outwards* from the OLR, while most of the [ILR, OLR] band is a forbidden band for density waves propagation. The wave that a slow halo linearly excites at its ILR (at large radius) can therefore naturally propagate inwards, and one does not need to invoke non-linear coupling to account for a disk response in the disk. Furthermore, non-linear coupling efficiency is weakened in the present situation with respect to a stellar disk. Indeed, non-linear coupling can be shown to be efficient whenever the resonances of partner waves coincide (for instance corotation and Lindblad resonance). A simple argument for that is that the waves spend a lot of time there, since their group velocities vanish, and they therefore have a large amount of time to exchange, non-linearly, a significant amount of energy and angular momentum. In a collisionless system the integral $\int_r^{r_{LR}} dr/c_g$ diverges, where r_{LR} is a Lindblad resonance location and c_g is the wave group velocity, which makes non-linear coupling a very efficient process in stellar disks (Tagger et al. 1987). In a non or weakly self-gravitating gaseous disk however, this integral is finite, and the non-linear coupling efficiency is therefore much lower with respect to a collisionless situation.

We shall assume hereafter that the dynamics of the H I disk of NGC 2915 can be adequately modeled with an isothermal gas disk in which the sound speed is equal everywhere to the observed velocity dispersion, assumed to be isotropic: $c_s \equiv \sigma_v$. Eq. (1) shows that once Ω_p is fixed, k (and therefore k_r) follows, as Ω, κ, Σ_g, and c_s are all observables. More precisely, k is given by a second-order polynomial equation admitting two roots, corresponding to the so-called long and short waves. In the regime where Q is high (i.e. when the term $-2\pi G\Sigma_g|k|$ is negligible), the two roots are very close to each other, and one can consider only the short wave.

k_r is related to the pitch-angle β of the spiral pattern by

$$\tan\beta = \frac{m}{k_r r}. \tag{2}$$

Therefore, given the observations and a guess at the pattern frequency of the perturber (and thus, in a forced regime, of the wave), Eqs. (1) and (2) directly yield the pitch angle of the spiral pattern. One thus only needs to adjust the perturber frequency to match the observed pitch angle, which can be estimated observationally by $\tan\beta_{\rm obs} = \frac{d\log r}{d\theta}$, where $r(\theta)$ traces the spiral arms and θ is the azimuthal angle in a deprojected map of the galaxy. The deprojected H I surface density of NGC 2915 in $(\log r, \theta)$ coordinates is shown in Fig. 3 for an inclination $i = 53\overset{\circ}{.}9$ (see below). From this image, we obtain $\beta_{\rm obs} \approx 7 - 10^\circ$ for the main feature at $2.3 \lesssim \theta \lesssim 4$ (mod. π), $r \approx 12$ kpc, and $\beta_{\rm obs} \gtrsim 20^\circ$ for the secondary features such as $1.8 \lesssim \theta \lesssim 2.6$ (mod. π), $6 \lesssim r \lesssim 11$ kpc.

In the linear regime, the wave amplitude (which does not appear in the dispersion relation) is independent of its pitch-angle. One can thus successively adjust the perturber pattern frequency and strength in order to match, respectively, the spiral pattern pitch-angle and arm-interarm contrast. In NGC 2915, however, the arm-interarm contrast is comparable to unity, the disk response is likely non-linear, and one cannot fit the perturber parameters (Ω_p and strength) by simply exploring the wave pitch-angle and arm-interarm contrast independently. The fit thus needs to be undertaken through numerical simulations.

The constraints discussed above can be used to estimate the best set of parameters for an external tidal perturber. In the second part of this paper, in which we investigate the behavior of a $Q \approx 1$ disk, the parameter space to be explored is different. It should also be noted that most of the torque from the perturbing potential is received by the disk at the Inner and Outer Lindblad resonances, where $\Omega = \Omega_p \pm \frac{\kappa}{m}$. The radial profile of the perturbing potential should thus only have a minor impact on the disk response. This greatly simplifies the exploration of parameter space, as it is not required to have a precise prescription of the perturber's shape and potential (unavailable anyway), and its strength can be adjusted simply by an adequate scaling (e.g. scaling the mass of a bar-like perturber or the triaxiality of a triaxial halo). Unfortunately, this simultaneously prevents any attempt to reach a detailed knowledge of the perturber's structure.

2.2. Constraints from the Velocity Field

For an infinitely thin disk, the observed (i.e. line-of-sight) velocity field of the gas flow can be expressed as:

$$v = [-u\cos(\theta - \varphi) + v\sin(\theta - \varphi)]\sin i, \tag{3}$$

where u and v are the radial and azimuthal components of the velocity in the galactocentric rest frame, i is the inclination, and θ and φ are, respectively, the azimuth of the fluid element under consideration and of the observer. The notation is illustrated in Fig. 4. Although the origin of azimuth can be chosen arbitrarily, it is traditionally chosen along the major axis of the galactic disk, on the receding side. For this choice of origin, $\varphi = -\pi/2$. As the velocity field associated with an m-folded density wave has an intrinsic $e^{im\theta}$ dependence in azimuth, one can easily see from Eq. (3) that it will lead to $m-1$ and $m+1$ folded signatures in the deprojected perturbed velocity field. Thus, the perturbed velocity field associated with an $m=2$ spiral will have $m=1$ and $m=3$ signatures when deprojected, and these can in principle be used to constrain the models.

Canzian (1993) showed that the weights of the $m=3$ to $m=1$ deprojected components increase steeply across corotation. This is true if the $m=1$ component of the observed velocity field comes only from the $m=2$ spiral pattern. However, in the case of NGC 2915, which is likely warped, this property does not hold and, as we shall see, we prefer to discard the $m=1$ information. More recently, Fridman et al. (2001) used the observed velocity information to reconstruct the velocity field of NGC 3631, and they underlined the important role of the $m=1$ and $m=3$ coefficients.

2.2.1. Case of the $m=1$ component:

The $m=1$ component of the deprojected velocity field can come from an $m=2$ perturbation to the velocity, but also from the $m=0$ component, i.e. the unperturbed circular rotation of the galactic disk. As soon as the inclination of the disk varies with radius, it is not possible to disentangle which fraction of the $m=1$ deprojected velocity comes from an $m=2$ density wave and which fraction comes from a warp. This corresponds to the infamous bias introduced in warped tilted ring models by so-called streaming motions, in this case horizontal $m=2$ perturbed velocities. Since the disk of NGC 2915 may be warped (Meurer et al. 1996), the $m=1$ component of the deprojected velocity field is not a suitable constraint for the simulations, and we will rather focus on the $m=3$ component. We thus neglect the possible warp of NGC 2915, but this not expected to alter significantly our conclusions, either qualitatively or quantitatively.

2.2.2. Case of the $m=3$ component:

The $m=3$ component of the deprojected velocity field can come from an $m=2$ perturbation to the velocity, such as an $m=2$ spiral density wave, as well as from an $m=4$ wave (which has $m=3$ and $m=5$ signatures). It can also arise from a wrong evaluation of the inclination (see Teuben 2002, and references therein). An error Δi on the inclination will lead to a $O(\Delta i)$ $m=1$ residual, but also to a weak $O(\Delta i^2)$ $m=3$ residual. Although the $m=3$ residual coming from an inclination error is weak ($\sim v_c\,\Delta i^2$), it is important to compare it with the $m=3$ residual coming from the bar or spiral perturbation, which is also small. Fig. 5 shows the radius-averaged value of this component as a function of the assumed inclination of the disk of NGC 2915 (Bureau et al. 1999 used $56 \pm 3°$). The solid line represents a second order polynomial fit to the data. One can easily check that the fit scales as $v_c\,\Delta i^2$, as expected.

Fig. 6 shows the amplitude of the $m = 3$ component of the deprojected velocity field (hereafter called $V_3^{\rm obs}$) as a function of radius, for three special values of the assumed inclination: $55\overset{\circ}{.}0$ (corresponding to the lowest data point in Fig. 5), $53\overset{\circ}{.}9$ (corresponding to the fit minimum), and $52\overset{\circ}{.}7$ (corresponding to the shape of the outermost isodensity contours, assuming circularity). These profiles do not markedly differ from each other, showing that the small uncertainty on the disk inclination has little impact on $V_3^{\rm obs}(r)$. A warp could affect this profile in a similar fashion to inclination uncertainty, but again the impact on the profile's shape should be minimal. We thus consider $V_3^{\rm obs}(r)$ an appropriate constraint for the simulations, where the equivalent profile $V_3^{\rm sim}(r)$ is easily constructed.

The $V_3^{\rm obs}(r)$ constraint is implemented as follows: we define the scalar product between two radial functions f and g as

$$\langle f|g\rangle = \int_0^{r_{\rm ext}} r f(r) g(r) dr, \tag{4}$$

and then search for the maximum of the function

$$\chi = \frac{\langle V_3^{\rm obs}(r)|V_3^{\rm sim}(r)\rangle}{[\langle V_3^{\rm obs}(r)|V_3^{\rm obs}(r)\rangle\langle V_3^{\rm sim}(r)|V_3^{\rm sim}(r)\rangle]^{\frac{1}{2}}} \tag{5}$$

in both time t and observer azimuth φ ($V_3(r)$ depends on φ), while keeping the inclination fixed at $53\overset{\circ}{.}9$. By construction, $|\chi|$ is always smaller than one, and it is exactly one if $V_3^{\rm obs}(r)$ and $V_3^{\rm sim}(r)$ are proportional (Schwarz's theorem). The closer $|\chi|$ is to unity, the more similar $V_3^{\rm obs}(r)$ and $V_3^{\rm sim}(r)$ are. In the linear regime, χ is independent of the amplitude of the perturbing potential, which can thus be optimized in a second step, matching $V_3^{\rm sim}(r)$ to $V_3^{\rm obs}(r)$ in both shape and absolute value.

It must be noted that the perturber's amplitude can be adjusted either by matching the amplitude of the perturbed velocity (i.e. $V_3^{\rm sim}(r)$) or by matching the amplitude of the perturbed density (i.e. the arm-interarm contrast). As indicated above, we adopted the first procedure. Naturally, the disk response should also match the perturbed density amplitude or the model must be discarded. The ratio of the perturbed velocity amplitude to the perturbed density amplitude depends not only on the wave frequency but also on the disk parameters. Given the simplifying assumptions made, we do not require a perfect simultaneous match, but simply that the arm-interarm contrast resembles the one observed. We also note that the r-weighting in Eq. (4) corresponds to a uniform weighting of the 2D deprojected map, and that the deprojected beam is elongated parallel to the minor axis at all points. The effect of beam smearing's resulting $m = 2$ modulation on $V_3^{\rm obs}(r)$ is not taken into account by our analysis, but it is likely to be small compared to the $m = 3$ component we are interested in. The integral in Eq. (4) should also have a lower limit at approximately one beam width. In practice, r-weighting and beam smearing tend to quash any $m \neq 0$ component at the center and thus make the integrand negligible for $0 < r \lesssim 45''$. One can therefore adopt either choice of lower limit.

2.3. Constraints from the Velocity Dispersion Field

We have now outlined how to take into account the constraints arising from the zeroth and first moments of the H I data cube (i.e. the column density and velocity fields). The second moment (i.e. the velocity dispersion field) is directly imposed to the model as the (azimuthally averaged) sound speed profile. We have also performed runs with a uniform sound speed $c_s \equiv 8$ km s^{-1}, as often observed in the outer parts of dwarfs, because the large central velocity dispersion could be partly due to beam smearing.

3. Hydrodynamic Code

The hydrodynamic code used is a simple 2D Eulerian finite difference program on a polar mesh written from scratch by one of us, and formerly used in another astrophysical context (protoplanet–protoplanetary disk tidal interactions). The mesh is staggered, that is to say the vertically integrated pressure and the surface density are zone centered, while the radial (resp. azimuthal) velocity is defined at the interface between two radially (resp. azimuthally) neighboring zones. The code solves discrete versions of the continuity and Euler equations, the different terms of which are treated sequentially through an operator splitting technique in much the same way as is done in ZEUS (Stone & Norman 1992). The algorithms used enforce mass and angular momentum conservation (for an isolated system) up to the computer accuracy. The advection is based on a second order upstream difference (van Leer 1977). There is no energy equation as the closure relation is provided by the observed velocity dispersion, treated here as the sound speed. This ensures that at any instant the simulated disk has a sound speed coinciding with the observed velocity dispersion. The drawback is that the disk quickly fragments into clumps at low Q. This does not happen in our externally forced disks, however, as the surface density is low. For our heavy disk models, where the gas surface density is scaled up, a work-around is discussed in § 5. As mentioned above, since beam smearing can result in an overestimated dispersion near the center, several velocity dispersion profiles have been tried with central values lower than observed. They all gave very similar results, except for the disk response near the center, which displays a relatively smooth but complex behavior at large σ_v and relatively strong shocks and a higher accretion rate onto the center for $\sigma_v \equiv 8$ km s^{-1}. These differences are of negligible importance, however, both in term of the χ value (our scalar product gives a small weight to the central parts by construction) or in terms of the beam convolved-synthetic maps. To relieve the Courant condition and increase the time step, azimuthal advection is treated so as to get rid of the average azimuthal velocity at each radius (Masset 2000a,b). In our case, however, the gain provided is relatively small since we have to deal with strong radial streaming at the center, where the disk response is bar-like. As we use a 2D code, we effectively neglect the galaxy warp.

For our external perturber models, the forcing is provided either by a bar or by a triaxial halo.

The bar models are characterized by the bar pattern speed Ω_p and its surface density

$$\Sigma(x,y) = \Sigma_b\left[\left(x^n + \frac{y^n}{q^n}\right)^{\frac{1}{n}}\right], \tag{6}$$

where x (respectively y) is measured along the bar major (respectively minor) axis, $q \equiv b/a \leq 1$ is the bar axis ratio, and n is a dimensionless index characterizing the shape of the bar isodensity contours. $\Sigma_b(r)$ is the bar density profile along its major axis, given by

$$\Sigma_b(r) = \Sigma_0 \exp(-r/h_b), \tag{7}$$

where Σ_0 is the bar central surface density and h_b its scalelength. The bar potential is thus entirely determined by the set of parameters h_b, q, n, and the total mass of the bar

$$M_{\rm bar} = \iint \Sigma(x,y)dxdy, \tag{8}$$

while its time behavior is determined by the pattern speed Ω_p. The exponential bar profile does not have a cut-off radius and the quadrupole term arising from it has a power-law rather than an exponential behavior. The bar elements located at $r \gg h_b$ nevertheless contribute negligibly to the bar potential itself, which is dominated by the contribution of the inner parts. We reemphasize that the detailed characteristics of the bar are unimportant for the disk tidal response (see § 2.1). The crude bar description provided by Eq. (6) is thus sufficient for our purposes.

In addition to the axisymmetric part of the bar potential, another $m = 0$ potential is applied to the disk in all of the bar forcing runs, so as to match the circular velocity curve. It can be interpreted as due to a spherical halo (which can not drive a wake in the H I disk).

The triaxial halo models are characterized by the halo pattern speed Ω_p and the ratio of the tangential to radial acceleration of an embedded test particle. The tangential acceleration has an $m = 2$ dependence in azimuth and the acceleration ratio was chosen either constant in radius or with dependences similar to the ones shown in Fig. 7. These acceleration ratios were obtained by computing the equatorial plane potential of ellipsoidal halos with isosurface-density axis ratios $a : b : c$ and major axis density profiles $\rho(r) \propto (1+(r/r_c)^2)^{-1}$. Varying c/a from 0.5 to 1.5 only has a small impact on these curves. The halo flattening is thus totally unconstrained by our models and we adopt $c \equiv a$ for all halo models.

The radial acceleration is derived from the observed circular velocity. Namely, we take the following prescription for the halo potential $\phi_{\rm halo}$:

$$\phi_{\rm halo}(r,\theta,t) = \phi_{m=0}(r) + \phi_{m=2}(r,\theta,t), \tag{9}$$

where

$$\phi_{m=0}(r) = -\int_r^{+\infty} \frac{v_c(r')^2}{r'}dr' \tag{10}$$

and

$$\phi_{m=2}(r,\theta,t) = \frac{1}{2}\mathcal{R}v_c(r)^2 \sin[2(\theta - \Omega_p t)], \tag{11}$$

with

$$\mathcal{R} = \left(0.34 + \frac{0.155}{1 + r/r_c}\right)\left(1 - \frac{b}{a}\right) \tag{12}$$

being the tangential to radial acceleration ratio (r_c is the halo core radius). Eq. (12) provides a satisfactory fit to the curves displayed in Fig. 7.

Self-gravity is taken into account in all simulations but the stellar content of NGC 2915 is neglected. The disk potential is evaluated through fast Fourier transforms (FFTs; see Binney & Tremaine 1987). Although potential evaluation with this technique is affected by numerical artifacts, the effect is unimportant in our case because self-gravity is weak (Q is large and the gas contribution to the total potential small).

4. External Perturber Models

4.1. Bar Forcing Runs

Figs. 8–10 show the best match results for a series of bar forcing runs. The pattern frequencies shown range from 5.0 to 7.5 km s^{-1} kpc^{-1} and the resolution was $N_r \times N_\theta = 100 \times 250$ for all runs, with an inner grid boundary $R_{\rm min} = 300$ pc and an outer boundary $R_{\rm max} = 25000$ pc, further than the edge of the observed H I disk to avoid spurious edge effects. The runs were performed in two steps. First, a tentative bar mass $M_b^0 = 5 \times 10^9\ M_\odot$ was adopted. The best match (both in time and observer's azimuthal angle φ; see § 2.2.2 for details) was then identified and the scaling ratio

$$\mathcal{S} = \frac{\int_0^{r_{\rm ext}} rV_3^{\rm sim}dr}{\int_0^{r_{\rm ext}} rV_3^{\rm obs}dr} \tag{13}$$

derived. A second run with bar mass $M_b = M_b^0/\mathcal{S}$ was then performed to match the $m = 3$ velocity profile in both shape and amplitude. The bar masses used for this second step are indicated in Tab. 1. The adopted axis ratio $q = 0.5$ and isophote shape index $n = 3$ are chosen from typical values found in the literature and do not represent extreme cases (Martin 1995; Freeman 1996). Fig. 8 shows a comparison of the $V_3^{\rm obs}$ and $V_3^{\rm sim}$ radial profiles for the best match of each run. Synthetic maps of the corresponding H I column density and line-of-sight velocity where also produced and are shown in Figs. 9 and 10, respectively. We note that since the external perturber has central symmetry, and since N_θ is an even number, the simulations can be run either on a full or half grid. We have adopted the latter. This is not a problem, however, as the simulations are not demanding on modern, cheap platforms, and the flow remains symmetric.

Contrary to our standard procedure (see § 2.3), the velocity dispersion for these runs was set to 8 km s^{-1} everywhere. As discussed above, a first series of runs using the observed velocity dispersion profile showed a non bar-like response and complex spiral structures in the center. When lowering the sound speed in the inner parts, one recovers the classical gas response in a bar-like potential, as shown in Figs. 8–10. The observed rise of the velocity dispersion in the central part of the galaxy could then be assigned to beam smearing, as the beam there intercepts kinematically independent regions, but this is rather unlikely (see § 4.2 and 5.2 in Meurer et al. 1996). The high central dispersion is almost certainly due to the burst of star formation. It may thus be that the central gas dynamics cannot be properly modeled with an isothermal gas, the sound speed of which corresponds to the observed velocity dispersion, or simply that the gas dynamics near the center is not dominated by the tidal forcing of a relatively slow, large-scale perturber. The initial setup is that for an unperturbed axisymmetric disk. Contrary to Athanassoula (1992b), the external perturber is not turned on slowly and a transient behavior is observed for the first few dynamical times.

We note that in the synthetic maps, the bar position angle is *not* adjusted; it is imposed by the best match observer's azimuth φ yielded by the $V_3^{\rm obs}(r)$ fitting (see Eq. 5). The fact that the modeled and observed bar position angles should coincide provides an additional constraint to the models. Figs. 8 and 9 show that the pattern speeds matching the $V_3^{\rm obs}$ profile and the column density map (with a satisfactory position angle for the bar) are relatively well constrained, $\Omega_p \approx 5.5 - 6.5$ km s^{-1} kpc^{-1}. For these forcing frequencies, however, the isovelocity contours north of the center exhibit a twist that is not observed (see Fig. 1; Meurer et al. 1996).

The difference between the observed and synthetic velocities could be interpreted as a kinematic warp, although its amplitude should be large to account for such a twist. The disk response in the central parts should not be too much of a concern, however, because of our poor knowledge of the true gas velocity dispersion there, as well as beam smearing effects on both the velocity and velocity dispersion maps. The frequency range $\Omega_p \approx 5.5 - 6.5$ km s^{-1} kpc^{-1} yields the right bar position angle and a satisfactory response in the outer disk, both in terms of perturbed surface density and streaming motions. However, the main spiral feature observed in Fig. 3 is not present in this series of runs. Fig. 11 shows the disk surface density in $(\log r, \theta)$ coordinates for the best bar forcing run, with $\Omega_p = 6.0$ km s^{-1} kpc^{-1}. The main characteristics of the observed distribution are recovered (end of the bar around $3 - 4$ kpc, pitch angle $\approx 20^\circ$ for the secondary outer features), but only a very faint structure with a low pitch-angle is present in the outer disk ($r \gtrsim 10$ kpc). To be fair, the observed H I disk of NGC 2915 is extremely clumpy and does not have a strict central symmetry. The bar-like structure is also clearly asymmetric and the pitch-angle estimate for the southern outer arm depends strongly on the H I clump at about $(-325'', +100'')$ in Fig. 1. Nevertheless, the residual velocity map does show mainly $m = 1$ and $m = 3$ components, strongly suggesting that, despite the departure of the H I column density map from central symmetry, the disk mainly owes its structure to a grand design $m = 2$ spiral wave.

Bar forcing runs have also been performed with higher and lower forcing frequencies than the ones presented here. For lower frequencies, the bar-like response of the disk becomes naturally longer and spreads over the whole disk. At higher frequencies, the bar becomes increasingly short and eventually vanishes, while the spiral response in the outer disk fades away. No value of the correlation coefficient χ close to unity is ever reached in these low and high frequency runs, so the perturber frequency is very well constrained. We also tried a series of runs in which the bar scalelength h_b was varied (inversely proportional to the pattern frequency), but no significant difference was found compared to the results already presented. Finally, runs with different q and n were done, again without fundamental differences to the set presented. The parameters M_b, q, n, and h_b are degenerate, i.e. different sets of values for these parameters can lead to the same quadrupole term at the bar Lindblad resonances, where the disk is torqued. More precisely, for a smaller bar mass, runs with slightly more extreme values of q and n yield a similar disk response at each forcing frequency.

The bars inferred from these runs must be dark. Indeed, the maximal mass one can assign to the optical component of NGC 2915 is $M_* \approx 7.4 \times 10^8\ M_\odot$ and the H I mass in the central bar is about $5 \times 10^7\ M_\odot$ (Meurer et al. 1996), to be compared to the bar masses derived in our runs of order $6 \times 10^9\ M_\odot$ (Tab. 1). This stellar mass is calculated using the circular velocity curve and the exponential fit to the optical image from Meurer et al. (1994), avoiding contamination by the bright, young central objects. The optical image further suggests that the stellar mass distribution is less elongated than the bars used in our runs, although both are roughly aligned. Increasing the bar axis ratio b/a while preserving the fit would require and even larger bar mass. The luminous component of NGC 2915 is thus totally unable to account for both the observed arm-interarm contrast and the streaming motions amplitude in the H I disk.

In fact, given the maximum contribution of the stars ($\lesssim 20$ km s^{-1} outside 2-3 kpc) and the gas (≈ 15 km s^{-1}) to the circular velocity curve (Meurer et al. 1996), it is not surprising that they are unable to produce non-circular motions of order 10 km s^{-1} (as required). In an unpublished manuscript, Quillen (1998) estimates the non-circular motions due to the gaseous bar at 2 km s^{-1} at most, much smaller than the observed H I velocity dispersion. The gas response should thus be smooth, unless a more massive non-axisymmetric component is present.

4.2. Triaxial Halo Runs

We have also performed a series of runs in which the disk response is excited by a rotating triaxial halo, as described in § 3, for the same set of pattern frequencies as the bar forcing runs discussed above. The runs were again performed in a two step procedure, first with an axis ratio $(b/a)_0 = 0.9$, then with

$$\frac{b}{a} = 1 - \frac{1}{\mathcal{S}}\left[1 - \left(\frac{b}{a}\right)_0\right]. \tag{14}$$

The axis ratios obtained for the second step vary between 0.83 and 0.88 for pattern frequencies between 4.5 and 9.5 km s^{-1} kpc^{-1}. The main characteristics of this set of runs are comparable to the bar forcing runs, so we do not show all the results explicitly. Fig. 12 shows the surface density response for a set of six different pattern speeds, at the best match timestep for each case.

Minor differences can be found compared to the bar forcing runs, but the bar position angle and length are in agreement and both sets display the same trends as the pattern speed is varied. The highest χ values are obtained for roughly the same forcing frequency range, but with slightly looser constraints ($6.5 \lesssim \Omega_p \lesssim 8.0$ km s^{-1} kpc^{-1}). Note in Fig. 12 that χ remains high up to the last plot, corresponding to $\Omega_p = 8.5$ km s^{-1} kpc^{-1}, while it drops to lower values for the following forcing frequency ($\Omega_p = 9.0$ km s^{-1} kpc^{-1}). Both the position angle of the bar and the spiral pattern are totally incompatible with observations for $\Omega_p = 8.5$ km s^{-1} kpc^{-1}, however, which explains why we restrain our estimate of plausible values of Ω_p to 8 km s^{-1} kpc^{-1}.

4.3. Discussion of the External Perturber Models

4.3.1. Perturber Frequency

We find that both our bar and halo forcing models can give rise to a well-developed spiral pattern in a disk modeled on that of NGC 2915. This is not a surprise, however, given that external bar-like potentials have long been known to excite spiral density waves in thin disks (e.g. Goldreich & Tremaine 1979). But it is interesting to note that the halo triaxiality needed to account for the observed non-circular motions is relatively mild, i.e. $b/a \approx 0.83 - 0.88$. The pattern frequency range inferred from our models is also consistent (within the errors) with the direct measurement by Bureau et al. (1999; $\Omega_p = 8.0 \pm 2.4$ km s^{-1} kpc^{-1}). The fact that the same perturber strength can simultaneously account for the arm-interarm contrast and the $V_3^{\rm obs}$ profile amplitude, and the fact that the $V_3^{\rm obs}$ profile fit implies an observer's azimuth yielding the correct bar position angle, both provide additional confidence in our models and show that the detailed spiral structure of NGC 2915 can be explained by an external driver. Although it lies at the center of the H I bar, the stellar component of NGC 2915 is too small and lightweight to represent the postulated bar-like perturber, and the spiral structure must be excited by an unseen component.

Orbit calculations indicate that self-consistent bars should end within their corotation radii (e.g. Contopoulos 1980; Athanassoula 1992a). This imposes in the case of NGC 2915 an upper limit on the bar pattern speed of $\Omega_p \lesssim 17.5$ km s^{-1} kpc^{-1} (for $r_b \approx 180'' = 4.6$ kpc; see Bureau et al. 1999). Furthermore, the general agreement from N-body simulations (e.g. Sellwood 1981; Athanassoula & Sellwood 1986) and observations (e.g. Athanassoula 1992b; see Elmegreen 1996 for a review) is that bars are fast, i.e. they end just inside corotation, with $r_{\rm cr}/r_b \approx 1.2$. This is clearly not the case here, but NGC 2915 is also of much later type than any of the objects considered so far. Although it is marginally rejected by our results, the H I bar in NGC 2915 could even end within its own inner Lindblad resonance (ILR), for which there is limited evidence in late-type bars (e.g. Combes & Elmegreen 1993; Elmegreen 1996). Our result of $\Omega_p = 6.0 \pm 0.5$ km s^{-1} kpc^{-1} implies a slow bar, with corotation near the edge of the observed H I disk ($r_{\rm cr}/r_b \approx 2.8$). This fact, together with NGC 2915's unusually dense and compact halo (see Meurer et al. 1996), is consistent with models of dark matter dominated (i.e. sub-maximal) barred galaxies, where bars transfer most of their angular momenta to the halos (e.g. Weinberg 1985; Debattista & Sellwood 1998). Unfortunately, most of these works considered collisionless (i.e. stellar only) systems, so it still remains to be clarified exactly how relevant all these mechanisms are in the case of NGC 2915.

Structure formation simulations in cold dark matter (CDM) scenarios have long argued for (strongly) triaxial dark matter halos around galaxies (e.g. Frenk et al. 1988; Dubinski & Carlberg 1991; Warren et al. 1992). These halos are supported by anisotropic velocity dispersions, tend to be prolate (although both the oblateness and triaxiality are slightly stronger in the outer parts), and have angular momenta preferentially aligned with the minor axis at all radii. Dissipation increases the oblateness but leaves the flattening unchanged (Dubinski 1994). More recent COBE-normalized ΛCDM simulations yield less flattened and less triaxial (i.e. more spherical) halos (Bullock 2002). The same tendency is observed as a function of decreasing mass and redshift. Jing & Suto (2002) also point out that the high density (central) regions of halos in ΛCDM universes are slightly more triaxial than the outer parts, but that highly concentrated halos tend to be rather spherical. This would argue against strong triaxiality in NGC 2915. The probability distributions obtained by Jing & Suto (2002) argue against a short-to-long axis ratio of $0.83 - 0.88$ (which is not "flattened" enough), but given this value a short-to-intermediate axis ratio of $0.83 - 0.88$ is most likely. Indications are that halos in warm and self-interacting dark matter simulations are even more spherical (Bullock 2002; Combes 2003). Observations of polar-rings, warps, and H I flaring suggest flattened halos around spiral galaxies (e.g. Sackett et al. 1994; Olling 1996; Becquaert & Combes 1997). There is also evidence for weak triaxiality (Franx & de Zeeuw 1992; Andersen et al. 2001), but it is rather contradictory in the case of elliptical galaxies (e.g. Franx, van Gorkom, & de Zeeuw 1994; Buote et al. 2002).

As far as we know, the figure rotation of the triaxial halos formed in CDM simulations has not been studied, beside the preliminary investigation presented in Bureau et al. (1999). However, the forcing pattern frequency inferred from our simulations is probably too high to be accounted for by a rotating triaxial halo. This can be shown by a simple calculation of the modified halo spin parameter λ', defined by Bullock et al. (2001) to be

$$\lambda' = \frac{J}{\sqrt{2}MVR}, \tag{15}$$

where J is the angular momentum inside a sphere of radius R (we neglect in this order of magnitude calculation the small triaxiality of the halo), containing a mass M, and $V = \sqrt{GM/R}$ is the circular velocity imposed by the halo at radius R. Bullock et al. (2001) find the log-normal statistics of the λ' parameter robust to the choice of R, so we choose here the disk outer radius, $R \approx 15$ kpc. The halo angular momentum up to R then reduces, summing on every dark particle i of mass m_i and distance to the center R_i, to the well known expression

$$J = \frac{2}{3}\Omega_p \sum_{i, R_i < R} m_i R_i^2, \tag{16}$$

where we have assumed spherical symmetry, and where we made the simplifying assumption that the motions of the dark particles in the rotating frame do not contribute sizably to J, i.e. that there are no net internal streaming motions in the rotating frame which could sizably modify our estimate of the halo angular momentum. One can thus write

$$\lambda' = \frac{\sqrt{2}\,\Omega_p \int_0^R \frac{dM}{dr} r^2 dr}{3MVR}. \tag{17}$$

Integrating by parts, and noting that according to our estimate of Ω_p the external perturber has its corotation at the edge of the H I disk (i.e. $\Omega_p R/V \approx 1$), one obtains

$$\lambda' = \frac{\sqrt{2}}{3}\left(1 - 2\int_0^1 x^2 \tilde{v}^2(x)dx\right), \tag{18}$$

where $x = r/R$ and $\tilde{v} = v_c/V$. Noting that $\tilde{v}(1) = 1$ and $\tilde{v}(x) < 1$ for $x < 1$ (i.e. the circular velocity curve reaches its maximum on $[0, R]$ at $r = R$), one obtains $1/3$ as a conservative lower limit for the bracket in Eq. (18). We thus have

$$\lambda' > \lambda'_{\rm min} = \sqrt{2}/9 \approx 0.157. \tag{19}$$

The statistics of λ' is a log-normal distribution,

$$P(\lambda') = \frac{1}{\lambda'\sqrt{2\pi}\sigma}\exp\left(-\frac{\log^2(\lambda'/\lambda'_0)}{2\sigma^2}\right), \tag{20}$$

with $\lambda'_0 = 0.035 \pm 0.005$ and $\sigma = 0.5 \pm 0.03$ (Bullock et al. 2001). If we adopt the most favorable values for our case, $\lambda'_0 = 0.04$ and $\sigma = 0.53$, the probability that a halo has a spin parameter as large as $\lambda'_{\rm min}$ or higher is only 5×10^{-3}. This probability drops to 1.6×10^{-4} if one takes the central values of $\lambda'_0 = 0.035$ and $\sigma = 0.5$ and if one uses the true behavior of $\tilde{v}(x)$ to estimate λ' from Eq. (18), which leads to $\lambda' \approx 0.212$. Consequently, if the spiral pattern of NGC 2915 is driven by an external perturber, it is unlikely that the perturber is a rotating triaxial halo, as this would imply that a considerable fraction of the halo total energy is in rotational kinetic energy ($\frac{1}{2}J\Omega_p$).

As stated, our estimate of J relies on the absence of net internal motions in the halo, which could sizably contribute to the halo angular momentum (although this need not be the case). A similar issue has been raised for stellar bars. Weinberg & Tremaine (1983) and Tremaine & Weinberg (1984b) report that a bar can have a negative effective moment of inertia. In our case, however, we need an almost exact cancellation of the solid body estimate by internal motions to bring the spin parameter down to plausible values, otherwise the order of magnitude of λ' is unchanged and our conclusions stand.

The alternative to the dark halo is a bar. Although unseen, this bar should not be made of dark matter, as one would again face the problem of excess angular momentum (see Christodoulou et al. 1995 and references therein). On the other hand, if the statistics of the spin parameter λ were to change, triaxial halos with figure rotation should then be expected to play a major role in galaxy formation and evolution, allowing for example the driving of non-axisymmetric structures in low surface brightness (LSB) galaxies.

Given that the total mass of NGC 2915 is smaller than most halos studied to date in CDM simulations ($\mathcal{M}_T \gtrsim 2.7 \times 10^{10}$ $M_\odot$; Meurer et al. 1996), it is of interest to study the expected scaling of the triaxial figure pattern frequency with the halo virial mass. An order of magnitude estimate for the former is:

$$\Omega_{\rm vir} \sim \frac{V_{\rm vir}}{R_{\rm vir}}, \tag{21}$$

which corresponds to the pattern frequency of a bar with half-length equal to the halo virial radius and $r_{\rm cr}/r_b = 1$. It should thus be considered the maximum figure pattern frequency for any halo with extended triaxiality. From Eq. (21), one can write

$$\Omega_{\rm vir}^2 \sim \frac{GM_{\rm vir}}{R_{\rm vir}^3}. \tag{22}$$

The virial mass can be expressed as

$$M_{\rm vir} = 200 \times \frac{4}{3}\pi R_{\rm vir}^3 \rho_{\rm crit}, \tag{23}$$

where the factor 200 depends only weakly upon the cosmology (see e.g. Navarro, Frenk, & White 1996) and $\rho_{\rm crit}$ is the critical density of the universe, linked to the Hubble constant H by

$$H^2 = \frac{8\pi G}{3}\rho_{\rm crit}. \tag{24}$$

Using Eqs. (22) to (24), one obtains

$$\Omega_{\rm vir} \sim 10H. \tag{25}$$

This result is independent of $M_{\rm vir}$, so that triaxial figure pattern frequencies should have statistics independent of the halo virial mass. Assuming $H = 70$ km s^{-1} Mpc^{-1}, one is led to $\Omega_{\rm vir} \sim 0.7$ km s^{-1} kpc^{-1}. The corresponding figure rotation time is $t_{\rm fig} = 2\pi/\Omega_{\rm vir} \sim 9$ Gyr. Interestingly, and although the details of the simulations are not mentioned, this frequency is in good agreement with the preliminary work presented by Bureau et al. (1999; $t_{\rm fig} \approx 5.5$ Gyr, see in particular their Fig. 10). The fact that this pattern frequency is an order of magnitude lower than that required to account for the spiral structure of NGC 2915 (if the latter is indeed driven by an external perturber) strengthens our conclusions that external forcing is unlikely.

4.3.2. Generic Models

Bekki & Freeman (2002) recently published a study of gaseous disks immersed in rotating triaxial halos modeled roughly on the situation in NGC 2915. However, they do not attempt to fit NGC 2915 in detail and only consider the gas surface density, not its velocities. Beside differences in the codes, they use a uniform sound speed $c_s \equiv 4$ km s^{-1}, a total gas mass an order of magnitude smaller than that in NGC 2915, and start with a uniform gas surface density. In that sense, their study is complementary to ours. Bekki & Freeman (2002) also find a strong dependence of the emerging disk structure on the perturber's frequency Ω_p, and their preferred values are consistent with ours (and thus also unlikely). Similarly, they find that the gas self-gravity and the scalelength of the dark halo are unimportant. Although their parameter space is too large to be well constrained (with five free parameters), they use an axial ratio $b/a = 0.8$, similar to the one we obtain for our triaxial halo runs. Bekki & Freeman (2002) also explored the effects of tilting the gas disk away from the equatorial plane of the halo. They find rich morphologies and kinematics which could be related to, e.g., polar rings and warps. Their runs also illustrate that tilting alone does not give rise to spiral arms, as is expected from the opposite vertical parities of the tilted halo perturbed potential and the spiral density wave, showing that triaxiality (with figure rotation) is essential.

5. Heavy Disk Models

The simulations performed in the previous section showed that the observations of NGC 2915 could be reasonably well accounted for by a grand-design spiral excited by an external perturber, the corotation of which would lie close to the edge of the H I disk. The nature of this unseen perturber is problematic, however, as a triaxial halo is unlikely to precess that fast, and the nature of a hypothetic bar that would otherwise act as a driver is unclear. Because the good agreements between the arm-interarm contrast, the $m = 3$ velocity perturbation amplitude and shape, and the bar position angle strongly support the observed spiral structure being a coherent grand-design pattern, and because the pattern speed of this spiral is both observationally and numerically constrained to have its corotation relatively close to the disk edge, it is tempting to suggest a global disk instability as an alternative explanation for the observed spiral structure. This requires the disk of NGC 2915 to be much more massive than what is inferred from H I column density measurements. As shown in Bureau et al. (1999), Toomre (1964, 1981) parameters $X(r) = r\kappa^2/2\pi m \mathrm{G}\Sigma$ and $Q(r) = c_s\kappa/\pi\mathrm{G}\Sigma$ are, for the (luminous) disk of NGC 2915, everywhere well above their critical values ($X \approx 3$ and $Q \approx 2$ for a flat rotation curve; see Toomre 1981). The idea that (some) dark matter is located in the disk is thus attractive since, in sufficient amount, it can decrease X and Q below their critical values and render the disk gravitationally unstable.

It is also well-documented that in many objects the H I surface density closely follows that of the total mass distribution. In the outer parts of galaxies, where dark matter dominates, H I thus traces the surface density of dark matter (see Bosma 1978, 1981; Broeils 1992a,b; Hoekstra, van Albada, & Sancisi 2001 for a recent study). As pointed out by Bureau et al. (1999), this is also true in NGC 2915 of the additional disk material required to bring X and Q to their critical values. The drawback is that by lowering Q, one would also expect to see wide-scale star formation in the disk, which is not observed (Bureau et al. 1999; Meurer et al. 1999). This must however depend on a number of parameters, including the nature of the disk dark matter, and it is unclear whether Kennicutt's (1989) star formation threshold can be applied directly to NGC 2915 (see § 5.3 for more on this issue). A number of independent lines of evidence also support massive disks and/or light low-concentration halos (see, e.g., Dubinski, Mihos, & Hernquist 1996, 1999 for the morphology of tidal tails). Furthermore, Fuchs (2002) recently showed that massive disks can account for the spiral structure observed in many LSB galaxies, bypassing the need for an external perturber (but raising the issue of the origin of such high $\mathcal{M}/L$ ratios). The support for disk dark matter thus remains non-negligible.

Pfenniger et al. (1994; see also Pfenniger & Combes 1994) discuss at length all the evidence in favor of rotationally supported (cold) disk dark matter. The underlying idea of their work is that most of the matter in disks is in the form of unseen cold molecular hydrogen. The disks are close to the threshold of Jeans instability and can develop some global disk gravitational spiral instability endowing them with a spiral structure at large scale, while at small scale they fragment into clumps inside which smaller scale fragmentation occurs, recursively, until a cut-off scale is reached (the "clumpuscule" scale).

The numerical description of a fractally fragmented heavy disk is an over-demanding problem ($Q \gtrsim Q_{\rm crit}$, where $Q_{\rm crit}$ is the critical value of the Toomre parameter below which the disk is gravitationally unstable; $Q_{\rm crit} = 1$ for an infinitely thin disk). The spatial and temporal dynamic ranges required from the simulations make it far beyond access of present computing resources, and one can only address the problem partially. Here, we tackle the problem of the global structure of a massive disk by starting with an axisymmetric disk at equilibrium, to which a small $m = 2$ seed is added. The gravitational potential is then filtered out at each timestep in order to retain only the large-scale $m = 0$, 2, 4, and 6 terms. We are thus able to follow a $Q \gtrsim Q_{\rm crit}$ disk large-scale dynamics over many rotation periods while avoiding the formation of small-scale clumps, the study of which is not relevant to our purposes. We filter out the $m = 1$, 3, and 5 terms because an initially axisymmetric system perturbed by a pure $m = 2$ seed should never display any odd-m modes, even in the non-linear stages. Indeed, as non-linear coupling of $m = 2p$ and $m' = 2q$ even modes lead to energy and angular momentum transfer into $m_{\rm nl} = m \pm m' = 2(p \pm q)$ modes, any perturbation which arises in the disk is always even folded (in other words, there is no spontaneous breakdown of the central symmetry). In our situation, we ensure this odd-m quiet behavior by filtering out odd modes at every time step.

5.1. Heavy Disk Simulations and Parameter Space

The heavy disk simulations use the same hydro-code as the external perturber simulations (see § 3 and 4), except for the aforementioned filtering of the gravitational potential. Furthermore, the observed gaseous surface density (Fig. 2) is scaled up by a uniform scalar $\lambda_\Sigma \geq 1$. As the spiral structure driver is now an instability internal to the disk, it is no longer necessary to invoke any external triaxiality and the resulting disk is embedded in a spherical halo. This halo radial density profile is constructed for each λ_Σ to match the observed circular velocity. We used the observed velocity dispersion profile (Fig. 2) directly and disregarded any possible beam smearing or other effects. The only free parameter is thus the dimensionless scalar λ_Σ, which we vary between 1 and 6, at which value Toomre's Q parameter is approximately unity at $r = 6.5$ and 9 kpc and the disk becomes globally unstable to axisymmetric modes (see Bureau et al. 1999). Our goal is to find the range of λ_Σ where a spiral instability develops, leading to the formation of a grand-design spiral structure similar to the one observed, and, if possible, to further constrain the value of λ_Σ so that the amplitude of the spiral also matches the observed one. We again use the observed $m = 3$ amplitude component of the deprojected velocity field as our main constraint, in a four step procedure:

1. For a given λ_Σ, we evaluate at each instant t the observer's azimuth φ that best fits the observed $V_3^{\rm obs}$ profile, i.e. we maximize the correlation coefficient χ defined by Eq. (5) for each t.
2. Given φ, we calculate the relative perturbation amplitude $\mathcal{S}(t)$ for each t, following Eq. (13).
3. We then compute the time average $\overline{\mathcal{S}}(\lambda_\Sigma)$ of $\mathcal{S}(t)$, discarding the first 750 Myr (a few dynamical times) when transient behavior is observed (see Fig. 13).
4. As $\overline{\mathcal{S}}(\lambda_\Sigma)$ should be unity in order to match the observed spiral structure in amplitude, we vary λ_Σ and repeat the procedure until a satisfactory value is found.

5.2. Heavy Disk Runs

Fig. 13 shows the relative amplitude of the spiral instability obtained as a function of the scaling ratio λ_Σ. $\overline{\mathcal{S}}(\lambda_\Sigma)$ depends dramatically on the scaling, allowing us to constrain λ_Σ accurately. The best match to the observed amplitude is obtained for $\lambda_\Sigma = 4.93$. Fig. 14 shows the corresponding density and velocity maps, as well as a comparison between $V_3^{\rm obs}(r)$ and $V_3^{\rm sim}(r)$. We again stress that the observer's azimuth in the three panels of Fig. 14 is the same, and that the position angle of the spiral structure is *not* adjusted but is imposed by the best match procedure. The corresponding χ value is 0.982. Fig. 15 shows the surface density response in $(\log r, \theta)$ coordinates. Although it is significantly different from the observed one in the center (less bar-like), the tightly wrapped spiral arms in the outer parts are well reproduced. In particular, the pitch angle measured for these spiral arms is about 7°, consistent with the observations and in contrast to the external forcing runs. Figs. 13–15 thus show that it is possible to account for most of the large-scale structure in the disk of NGC 2915 by simply scaling up uniformly the observed gas surface density.

Before inferring from this calculation the actual mass that has to be in the disk of NGC 2915, if it indeed owes its spiral structure to gravitational instabilities, it is important to estimate the impact of finite thickness. The grid over which we compute the potential has everywhere a zone size much smaller than the estimated disk thickness. The computed potential is thus that of an infinitely thin disk with surface density $\Sigma_{\rm thin}(r,\theta)$. This potential, filtered out in m, can be written as

$$\phi_{\rm thin}(r,\theta) = \phi_0^{\rm halo}(r) + \phi_0^{\rm disk}(r) + \sum_{n=1}^{3} \phi_{2n}^{\rm disk}(r,\theta), \tag{26}$$

where $\phi_m^{\rm disk}(r,\theta)$ is the $m-$th Fourier component of the infinitesimally thin disk's potential. On the other hand, for a moderately thick (i.e. $H \ll r$, where H is the characteristic thickness) but vertically resolved disk with the same surface density, the potential expression would read

$$\phi_{\rm resolved}(r,\theta) = \phi_0^{\rm halo}(r) + \phi_0^{\rm disk}(r) + \sum_{n=1}^{3} q\,\phi_{2n}^{\rm disk}(r,\theta), \tag{27}$$

where q is a correction factor, the expression of which is $q \approx (1+kH)^{-1}$ (Vandervoort 1970; Romeo 1992; k is again the wave-vector). Using Eq. (2) and writing $k_r \approx k$ (since $m=2$ is small) yields

$$q \approx \left(1 + \frac{2\sigma_v}{v_c \tan\beta}\right)^{-1}. \tag{28}$$

A thin but vertically resolved disk, leading to the same perturbed potential as computed for our heavy disk runs, should therefore have a surface density

$$\Sigma_g'(r) = \frac{\lambda_\Sigma}{q}\Sigma_g. \tag{29}$$

In the outer disk of NGC 2915, assuming $\sigma_v = 8$ km s^{-1}, $v_c = 80$ km s^{-1}, and $\beta = 10°$, $q = 0.47$, while $q = 0.65$ for $\beta = 20°$. In the inner disk, the wave becomes more open ($\tan\beta$ increases) but the circular velocity decreases. We thus adopt for the sake of simplicity a uniform value for our runs, $q = 0.5$. This is obviously a crude assumption and is the main source of uncertainty when computing the required disk surface densities (much more than the small uncertainty on λ_Σ). For such a disk, the fraction of the axisymmetric part of the potential due to the disk is $q^{-1} \approx 2$ larger than in our runs, but since the halo is constructed afterward to fit the observed circular velocity, the dynamics is not affected (the total axisymmetric component of the potential $\phi_0(r) = \phi_0^{\rm halo}(r) + \phi_0^{\rm disk}(r)$ remains unchanged). We can construct a modified halo profile using the observed circular velocity curve, from which we subtract the contribution of a disk with surface density profile given by Eq. (29) (i.e. about ten times more massive than the observed gaseous disk). The result for our best heavy disk model with $\lambda_\Sigma = 4.93$ is shown in Fig. 16.

Fig. 16 also shows that the disk and halo circular velocities, and thus their integrated masses, are roughly equal over most of the disk. This result depends on the adopted value for the correction factor but remains qualitatively unchanged as long as the correction factor parameter $q \lesssim 0.65$. For $q = 0.7$, the halo dominates by a factor of 2 at $r = 10$ kpc and more further out. The equality of disk and halo masses is in agreement with recent structure formation simulations including gas cooling in standard ΛCDM cosmologies (Teyssier, priv. com.; see also Teyssier 2002). Although the stellar component of NGC 2915 has been neglected in all simulations, we do not expect any sizable consequences on our result, as the curves in Fig. 16 would only need to be modified in the inner few kiloparsecs. More precisely, as our models respect the observed circular velocity profile, the optical component of NGC 2915 is effectively incorporated in the halo.

We saw in Fig. 14 that the spiral pattern obtained differs somewhat from the observed one. In particular, the spiral arms occur at a radius slightly smaller than observed and the central condensation has a stronger $m = 4$ symmetry. Nevertheless, the agreement between the $\lambda_\Sigma = 4.93$ model and the observations is satisfactory considering the small dimensionality (1) of the parameter space. We stress that any $m = 4$ spiral density wave would have an effect on the $m = 3$ deprojected velocity field, so that the simulated $V_3^{\rm sim}$ profile could arise from a mixture of $m = 2$ and $m = 4$ waves. In this run, however, we find that the outer spiral structure is the superposition of two $m = 2$ spiral density waves with different pattern speeds. The main wave has $\Omega_p = 6.0$ km s^{-1} kpc^{-1}, consistent with the direct measurement of Bureau et al. (1999), and corresponding to a corotation close to the disk edge. The second wave has $\Omega_p \approx 10$ km s^{-1} kpc^{-1} but is not well determined, as the perturbed density power spectrum deduced from the simulation is relatively noisy.

5.3. Discussion of the Heavy Disk Models

Not surprisingly given our motivations for doing so, we find that scaling up the gas surface density of NGC 2915 gives rise to a well-developed spiral pattern. Our heavy disk model also provides a satisfactory fit to NGC 2915's column density map and velocity perturbations. The corrected scaling factor $\lambda_\Sigma/q \approx 10$ we obtain is in good agreement with those derived for a variety of spiral galaxies, where typical values are $6 - 10$ with a tail at larger values (e.g. Hoekstra et al. 2001; Combes 2003; $\lambda_\Sigma/q = \Sigma_{\rm dark}/\Sigma_g + 1 = 3/4\,(\Sigma_{\rm dark}/\Sigma_{HI}) + 1$). Swaters (1999) obtains slightly lower factors for his sample of (gas-rich) late-type dwarfs, but again a tail of high values is present.

We note however that the above values are normally determined by attempting to fit the circular velocity curve only (with a scaled-up H I+He disk and a stellar component with free $\mathcal{M}/L$), while our goals here differ and we allow for an extra dark halo. Such circular velocity curve fitting would yield a scaling factor of about 25 for NGC 2915 (neglecting the stellar component, which is safe here), but as can be seen from Fig. 16 it would poorly reproduce the total circular velocity. Wiggles in the predicted circular velocity curve are not present in the observed one, requiring a smoother dark disk material distribution for improved fitting. Furthermore, in NGC 2915, the scaling factor obtained from the circular velocity curve is much higher than that obtained from the requirement of spiral structure sustainability, and the resulting disk would be violently unstable to axisymmetric perturbations (see below). This strongly argues for the presence of a classical (i.e. spherical or near-spherical) dark matter halo in addition to any realistic massive disk. A similar argument could be made based on the number of spiral arms in the disk (e.g. Athanassoula, Bosma, & Papaioannou 1987). As pointed out by Hoekstra et al. (2001), a circular velocity curve remaining flat significantly outside of the observed range would normally make the fit of a scaled-up gaseous disk alone progressively more difficult, but this is not the case here as the circular velocity curve predicted from the H I is still slightly rising in the outer parts.

The adopted scaling of the gas surface density brings the disk of NGC 2915 close to the critical value of the Toomre parameter, for which the disk is unstable to axisymmetric modes and fragments ($Q_{\rm crit} \approx 0.5$ for a vertically resolved disk). It is therefore interesting to compare the surface density profile of NGC 2915 with Kennicutt's (1989) threshold for the onset of star formation, as the disk is not observed to form stars. Kennicutt's critical surface density is defined by

$$\Sigma_c(r) = \alpha \frac{\kappa \sigma_v}{3.36G}, \tag{30}$$

where $\alpha = 0.67$. This critical surface density corresponds to the marginal stability of a thin gas layer embedded in a more massive, thicker stellar disk to two-component (fluid and collisionless) axisymmetric instabilities (see Rafikov 2001 and references therein). If we adapt this criterion (marginal stability) to the present situation, for which $Q(r) = \kappa\sigma_v/\pi G\Sigma$ and $Q_{\rm crit} \approx 0.5$, the critical surface density becomes

$$\Sigma'_c(r) = \frac{2\kappa\sigma_v}{\pi G} \approx 3.2\,\Sigma_c(r). \tag{31}$$

We note that although our scaling adds another fluid to the disk of NGC 2915, it is indistinguishable from the H I as the same sound speed is assumed, and we recover the one-fluid stability criterion. Indeed (see e.g. the $R = 1$ dotted line in Fig. 3 of Rafikov 2001), the stability criterion reads $1/Q_{\rm disk\ DM} + 1/Q_{\rm HI} = 1/Q_{\rm crit}$ (where we replaced 1 by $1/Q_{\rm crit}$ to account for the vertical thickness), leading to $\pi G(\Sigma_{\rm disk\ DM} + \Sigma_{\rm HI})/c_s\kappa = 1/Q_{\rm crit}$ and to Eq. (31), where $\Sigma'_c(r)$ refers to the *total* (i.e. dark matter + H I) disk surface density.

The two critical surface densities given by Eqs. (30) and (31) are compared with that inferred from our best match heavy disk model in Fig. 17, where we use the observed velocity dispersion profile $\sigma_v(r)$. According to the standard criterion (also used by Bureau et al. 1999), the disk would be expected to form stars at almost all radii, whereas according to the modified criterion it is not expected to form stars at all. This should not come as a surprise, however, since the modified criterion comes from the same marginal stability argument underlying our massive disk models, where we simply scaled up the observed gas surface density, approaching the limit of gravitational instability without ever reaching it. The correction factor $q = 0.5$ used to infer the surface density of a vertically resolved disk is the same as the marginally (un)stable Q value for a vertically resolved gaseous disk, explaining why the heavy disk surface density profile is everywhere close to but smaller than $\Sigma'_c(r)$. The non-prediction of star formation within $r \approx 3.5$ kpc, even with the standard threshold, should not be taken too seriously since we have neglected the stellar component of NGC 2915, which extends to about 3 kpc (Meurer et al. 1994).

It should be noted that the scaling factor $\lambda_\Sigma/q \approx 10$ inferred from our heavy disk models depends on the assumed distance D to NGC 2915. Since the observed Toomre Q parameter scales as D^{-1}, a smaller scaling ratio would be needed if the galaxy were further than estimated by Meurer et al. (1996; our adopted distance of 5.3 ± 1.6 Mpc). However, an order of magnitude increase in the distance would be needed to reach $Q(r) \approx 0.5$, which seems highly unlikely. Nevertheless, an improved distance determination would be helpful, for example from Cepheids or the tip of the red giant branch with HST. Quillen (1998) discussed in detail the issue of NGC 2915's distance. While she considers an increase of the distance by a factor of 2 unlikely but possible, her arguments would completely reject an increase by a factor of 10.

We also stress that Q, and thus λ_Σ, also depend on the assumed velocity dispersion of the additional disk material. For the sake of simplicity and in order to keep our parameter space as small as possible, we have assumed that the unseen material is tightly linked to the observed H I and has the same velocity dispersion and (consistently) the same vertical extent. Less additional material would be needed if it had a lower velocity dispersion. Indeed, the ratio c_s/Σ_g (or σ_v/Σ_g) is degenerate in the expression of Q. A change of order unity in Q_{crit} would also be expected to account for two-component axisymmetric (in)stability, and other two-components instabilities may develop (Rafikov 2001).

6. Discussion and Conclusions

We have performed 2D hydrodynamic simulations of the galaxy NGC 2915 in order to find a plausible explanation for the spiral structure observed in its extended H I disk. We have explored two main hypotheses: i) the observed bar/spiral structure is excited by an external driver, which we assume to be either a rotating bar or triaxial halo, and ii) the observed structure is due to a gravitational instability in the disk, which would contain an important unseen component and be much more massive than currently inferred from H I observations. In the first case, the free parameters are the external driver pattern frequency and strength (bar mass or halo triaxiality). Our results constrain the pattern frequency to $\Omega_p \approx 5.5 - 6.5$ km s^{-1} kpc^{-1} and the bar mass and halo axis ratio to $M_{\rm bar} \approx 5 - 7 \times 10^9$ $M_\odot$ and $b/a \approx 0.83 - 0.88$, respectively. However, based on current structure formation simulations, it is unlikely that a triaxial halo would have such a fast figure rotation (the spin parameter λ is too large), while the mass required for the bar is at least an order of magnitude larger than the optical mass of the central galaxy. All our external driver models also fail to reproduce the small spiral arms pitch angle observed in the outer disk. The external perturber model is thus implausible and we do not favor it. In the heavy disk case, the only free parameter is the disk surface density scaling ratio. We found that a (corrected) scaling ratio of about 10 leads to a spiral instability adequately accounting for the disk spiral structure and non-circular motions: the spiral pitch angle and arm-interarm contrast are accurately reproduced. The scaling ratio is well constrained by the simulations and the main uncertainty arises from the correction factor of the perturbed potential (to account for finite thickness). A scaling ratio of 10 yields roughly the same amount of disk matter and halo dark matter over the disk radius while the halo dominates further out. This is consistent with recent ΛCDM structure formation simulations. Furthermore, given that the heavy disk model reproduces the perturbed velocities and leads to a redistribution of angular momentum, an external triaxial potential is not required to explain the fueling of the central BCD starburst. Even for such a heavy disk, Kennicutt's (1989) star formation criterion is valid and accounts for the absence of star formation in the disk of NGC 2915, provided it reads as $Q > Q_{\rm crit}$, where $Q_{\rm crit}$ is the critical value of the Toomre parameter for the onset of Jeans instability. As the disk of NGC 2915 does not lie in the equatorial plane of a more massive, thicker stellar disk, the expression of $Q_{\rm crit}$ is different from that of standard galactic gaseous disks.

Throughout this work, we have neglected a possible warp in NGC 2915, we have assumed that the observed velocity dispersion could be adequately modeled as the sound speed of an isothermal gas, and we have not considered the small-scale clumpy structure present at the beam scale in the H I observations. We have also assumed, respectively, a unique external driver pattern frequency and a uniform disk surface density scaling ratio, in order to keep the dimensionality of our parameter space as small as possible. As such, our study is exploratory in nature. This might in turn lead to too crude a description of NGC 2915, and relaxing one or several of these assumptions may be required to improve the fit. For our heavy disk models, we also assumed a non-responsive spherically symmetric halo, whereas the disk mass is comparable to the halo mass within its radius. Considering a live halo thus appears a priority for any further similar modeling. It should in particular improve the fit to the observed central bar-like structure, where our current model fails.

Although we favor the heavy disk model over an external perturber, both models fail to reproduce satisfactorily the gas response in the center. Perturber models can loosely reproduce the bar-like feature observed but are unable to account for the kinematic twists, while heavy disk models simply fail to generate bar-like structures. The complexity of the central dynamics is in any case probably much greater than our models allow, and it is likely for instance that a different forcing frequency has to be considered for the central regions. In addition, the heavy disk models do not include any interaction or feedback from the stars, which could initiate the bar-like response. Despite a poor description of the central regions, we emphasize that a satisfactory description of the outer disk ($4.6 < r < 15$ kpc) is obtained, simultaneously in terms of perturbed velocity and perturbed density, with a very restricted set of adjustable parameters (2 in the forced runs, 1 for the heavy disks). Furthermore, only the heavy disk models properly account for the observed small pitch angle of the spiral arms. This strong constraint thus favors this latter set of models.

If one adopts the massive disk interpretation, NGC 2915 appears as an aborted optical grand-design spiral because its gas layer has not reached the critical surface density for star formation. The spiral pattern is nevertheless present because the surface density is *just* under this threshold. We recall however that there is a degeneracy between the surface density and velocity dispersion of the dark disk material. A long-standing and possibly related issue is how the H I velocity dispersion can remain at ≈ 8 km s^{-1} in the outer disk, without any obvious thermal or mechanical energy source. In particular, the question whether the observed spiral density wave could constitute a sufficient heating source for the disk material should be addressed (whether due to an external driver or to a gravitationally unstable massive disk).

It is interesting to note that if, in any isolated object, the increased disk surface density required to explain the existence of a spiral pattern were to over-predict the observed circular velocity curve, then disk dark matter (exclusively) could be ruled out as the source of that pattern, leaving a rotating triaxial halo as the most likely source. Undisturbed LSB galaxies which are not dark matter dominated and show a clear spiral structure would be ideal candidates for such a test. However, it is not clear whether such objects exist. Spiral-based scaling factors in LSB galaxies generally produce maximum disk velocities that are high but still within the maximum allowed by the circular velocity curve (e.g. Fuchs 2002).

Support for this work was provided by NASA through Hubble Fellowship grant HST-HF-01136.01 awarded by the Space Telescope Science Institute, which is operated by the Association of Universities for Research in Astronomy, Inc., for NASA, under contract NAS 5-26555. The authors wish to thank G.R. Meurer for NGC 2915's data and the organizers of the Guillermo Haro Workshop held in Puebla, Mexico, in May 2001, which was the starting point of this collaboration. F.M. wishes to thank R. Teyssier and P.-A. Duc for valuable discussions. M.B. similarly acknowledges useful discussion with K.C. Freeman. J. van Gorkom, F. Combes and E. Athanassoula are also thanked for reading and commenting on a first draft of the manuscript. The Digitized Sky Surveys were produced at the Space Telescope Science Institute under U.S. Government grant NAG W-2166. The images of these surveys are based on photographic data obtained using the Oschin Schmidt Telescope on Palomar Mountain and the UK Schmidt Telescope. The plates were processed into the present compressed digital form with the permission of these institutions. This research has made use of NASA's Astrophysics Data System Bibliographic Services.

REFERENCES

Andersen, D. R., Bershady, M. A., Sparke, L. S., Gallagher, J. S., III, Wilcots, E. M. 2001, ApJ, 551, 131

Athanassoula, E. 1992a, MNRAS, 259, 328

———. 1992b, MNRAS, 259, 345

Athanassoula, E., Bosma, A., & Papaioannou, S. 1987, A&A, 179, 23

Athanassoula, E., & Sellwood, J. A. 1986, MNRAS, 221, 213

Becquaert, J.-F., & Combes, F. 1997, A&A, 325, 41

Bekki, K., & Freeman, K. C. 2002, ApJ, in press. (astro-ph/0206208)

Binney, J., & Tremaine, S. 1987, Galactic Dynamics (Princeton: Princeton Univ. Press)

Bosma, A. 1978, Ph.D. Thesis, University of Groningen

———. 1981, AJ, 86, 1791

Broeils, A. H. 1992, A&A, 256, 19

———. 1992, PhD Thesis, Rijksuniversiteit Groningen

Bullock, J. S. 2002, in The Shapes of Galaxies and their Halos, ed. P. Natarajan (World Scientific), in press. (astro-ph/0106380)

Bullock, J. S., Dekel, E., Kolatt, T. S., Kravtsov, A. V., Klypin, A. A., Porciani, C., & Primack, J. R. 2001, ApJ, 555, 240

Buote, D. A., Jeltema, T. E., Canizares, C. R., & Garmire, G. P. 2002, ApJ, in press. (astro-ph/0205469)

Bureau, M., Freeman, K. C., Pfitzner, D. W., & Meurer, G. R. 1999, AJ, 118, 2158

Byrd, G., Rautiainen, P., Salo, H., Buta, R., & Crocker, D. A. 1994, AJ, 108, 476

Canzian, B. 1993, ApJ, 414, 487

Christodolou, D. M., Kazanas, D., Shlosman, I., & Tohline, J. E. 1995, ApJ, 446, 472

Combes, F. 2003, NewAR, in press. (astro-ph/0206126)

Combes, F., & Elmegreen, B. G. 1993, A&A, 271, 391

Contopoulos, G. 1980, A&A, 81, 198

Debattista, V. P., & Sellwood, J. A. 1998, ApJ, 493, L5

Dubinski, J. 1994, ApJ, 431, 617

Dubinski, J., & Carlberg, R. G. 1991, ApJ, 378, 496

Dubinski, J., Mihos, J. C., & Hernquist, L. 1996, ApJ, 462, 576

———. 1999, ApJ, 526, 607

Elmegreen, B. 1996, in Barred Galaxies, eds. R. Buta, D. A. Crocker, & B. G. Elmegreen (San Francisco: ASP), 197

Franx, M., van Gorkom, J. H., & de Zeeuw, T. 1994, ApJ, 436, 642

Franx, M., & de Zeeuw, T. 1992, ApJ, 392, 47

Freeman, K. 1996, in Barred Galaxies, eds. R. Buta, D. A. Crocker, & B. G. Elmegreen (San Francisco: ASP), 1

Frenk, C. S., White, S. D. M., Davis, M., & Efstathiou, G. 1988, ApJ, 327, 507

Fridman, A. M., Khoruzhii, O. V., Polyachenko, E. V., Zasov, A. V., Sil'Chenko, O. K., Moiseev, A. V., Burlak, A. N., Afanasiev, V. L., et al. 2001, MNRAS, 323, 651

Fuchs, B. 2002, in IVth International Conf. on Dark Matter in Astro and Particle Physics, eds. H. V. Klapdor-Kleingrothaus, & R. Viollier, in press. (astro-ph/0204387)

Goldreich, P., & Tremaine, S. 1979, ApJ, 233, 857

Hoekstra, H., van Albada, T. S., & Sancisi, R. 2001, MNRAS, 323, 453

Jing, Y. P., & Suto, Y. 2002, ApJ, in press. (astro-ph/0202064)

Kennicutt, R. C., Jr. 1989, ApJ, 344, 685

Lin, C. C., & Shu, F. H. 1964, ApJ, 140, 646

Masset, F. S. 2000a, A&AS, 141, 165

———. 2000b, in Disks, Planetesimals and Planets, eds. F. Garzón, C. Eiroa, D. de Winter, and T. J. Mahoney, 75

Masset, F., & Tagger, M. 1997, A&A, 318, 747

Martin, P. 1995, AJ, 109, 2428

Meurer, G. R., Carignan, C., Beaulieu, S. F., & Freeman, K. C. 1996, AJ, 111, 1551

Meurer, G. R., Freeman, K. C., Bland-Hawthorn, J., Jones, M. R., Knezek, P. M., & Allen, R. J. 1999, BAAS, 31, 828

Meurer, G. R., Mackie, G., & Carignan, C. 1994, AJ, 107, 2021

Navarro, J. F., Frenk, C. S., & White, S. D. M. 1996, ApJ, 462, 563

Noguchi, M. 1987, MNRAS, 228, 635

Olling, R. P. 1996, AJ, 112, 481

Pfenniger, D., & Combes, F. 1994, A&A, 285, 94

Pfenniger, D., Combes, F., & Martinet, L. 1994, A&A, 285, 79

Quillen, A. C. 1998 (astro-ph/9801217)

Rafikov, R. R. 2001, MNRAS, 323, 445

Romeo, A. B. 1992, MNRAS, 256, 307

Sackett, P. D., Rix, H.-W., Jarvis, B. J., & Freeman, K. C. 1994, ApJ, 436, 629

Schwarz, M. P. 1981, ApJ, 247, 77

———. 1984, MNRAS, 209, 93

Sellwood, J. A. 1981, A&A, 99, 362

Stone, J. M., & Norman, M. L. 1992, ApJS, 80, 753

Swaters, R. 1999, PhD Thesis, Rijksuniversiteit Groningen

Tagger, M., Sygnet, J.-F., Athanassoula, E., & Pellat, R. 1987, ApJ, 318, 43

Teyssier, R. 2002, A&A, 385, 337

Teuben, P. J. 2002, in Disks of Galaxies: Kinematics, Dynamics and Perturbations, eds. E. Athanassoula & A. Bosma (San Francisco: ASP), in press. (astro-ph/0204471)

Toomre, A. 1964, ApJ, 139, 1217

———. 1981, in Structure and Evolution of Normal Galaxies, eds. S. M. Fall & D. Lynden-Bell (Cambridge: Cambridge University Press), 111

Tremaine, S., & Weinberg, M. D. 1984, ApJ, 282, L5

———. 1984, MNRAS, 209, 729

Vandervoort, P. O. 1970, ApJ, 161, 87

van Leer, B. 1977, J. Comput. Phys., 23, 276.

Warren, M. S., Quinn, P. J., Salmon, J. K., & Zurek, W. H. 1992, ApJ, 399, 405

Weinberg, M. D. 1985, MNRAS, 213, 451

Weinberg, M. D., & Tremaine, S. 1983, ApJ, 271, 586

This preprint was prepared with the AAS LaTeX macros v5.0.

Fig. 1.— First two moments of the H I distribution in NGC 2915 (natural weighting). *Top:* Grey scale image of the total H I map (moment 0). *Bottom:* Mean H I velocity field (moment 1) overlaid on an optical image from the Digitized Sky Survey. The velocities are relative to the systemic velocity of NGC 2915, the velocity resolution is 6.6 km s^{-1}, and the contours are spaced by 10 km s^{-1}. The beam is $45'' \times 45''$ in both maps and drawn to scale in the top right corner of each panel. Adapted from Meurer et al. (1996) with permission.

Fig. 2.— Azimuthally averaged radial profiles of NGC 2915. *Left:* Gas surface density Σ_g. *Center:* Circular velocity v_c (rotation curve corrected for asymmetric drift). *Right:* H I velocity dispersion σ_v. The profiles are based on uniformly-weighted data ($25''$ beam) for $r \lesssim 10$ kpc and naturally-weighted data ($45''$ beam) at larger radii.

Fig. 3.— Gas surface density of NGC 2915 in $(\log r, \theta)$ coordinates, obtained by assuming an inclination $i = 53\overset{\circ}{.}9$ and scaling the deprojected H I surface density by 4/3.

Fig. 4.— Sketch of the notation used in the text (§ 2.2).

Fig. 5.— Average amplitude of the $m = 3$ component of the deprojected velocity field of NGC 2915, as a function of the assumed galactic inclination ($140 \leq r \leq 385''$). The solid line shows a second order polynomial fit to the data, represented by diamonds. The vertical lines mark the inclinations used in Fig. 6.

Fig. 6.— Amplitude of the $m = 3$ component of the deprojected velocity field of NGC 2915, as a function of radius, for three different values of the assumed galactic inclination. *From top to bottom:* $i = 55\overset{\circ}{.}0$, $53\overset{\circ}{.}9$, and $52\overset{\circ}{.}7$. The data are truncated at half the beam size.

Fig. 7.— Radial profile of the tangential to radial acceleration ratio for four different triaxial halos. *From top to bottom:* $b/a = 0.7$, 0.8, 0.9, and 0.95. All halos have $c/a = 1$ and a core radius $r_c = 2$ kpc.

Fig. 8.— Amplitude of the $m = 3$ component of the deprojected velocity field, as a function of radius for our best bar forcing runs. Solid lines show the best match in each case; dotted lines represent the observations. The pattern frequency Ω_p and correlation coefficient χ are indicated in the top-right corner of each panel. Contrary to Figs. 9 and 10, these data were not convolved by the beam.

Fig. 9.— Synthetic column density maps for our best bar forcing runs (see Fig. 8). The timestep and pattern frequency are indicated in each panel. Convolution by a beam size of $45''$ has been applied.

Fig. 10.— Synthetic velocity fields for our best bar forcing runs (see Figs. 8 and 9). The timestep and pattern frequency are indicated in each panel. Convolution by a beam size of $45''$ has been applied.

Fig. 11.— Deprojected surface density of the bar forcing run with $\Omega_p = 6.0$ km s^{-1} kpc^{-1}, in $(\log r, \theta)$ coordinates, at the best match time. Convolution by a beam size of 45$''$ has been applied.

Fig. 12.— Synthetic column density maps for our best halo forcing runs The timestep and pattern frequency are indicated in each panel. Convolution by a beam size of 45$''$ has been applied.

Fig. 13.— Relative amplitude of the spiral instability for the heavy disk models. *Left:* Time averaged relative amplitude $\overline{\mathcal{S}}(\lambda_\Sigma)$ as a function of the surface density scaling ratio λ_Σ. *Right:* Time dependence of $\mathcal{S}(t)$ for various values of λ_Σ (identified by squares in the left panel). *From top to bottom:* $\lambda_\Sigma = 5.2$, 5.0, 4.93, 4.85, 4.5, 4.0 and 3.5. The time behavior for $\lambda_\Sigma = 5.5$ is not shown as the disk is very close to $Q = 1$ and fragments into two large symmetrical clumps. The $\lambda_\Sigma = 4.93$ curve, identified by a thick line, is the best match model presented in this section and has the average relative amplitude $\overline{\mathcal{S}}(\lambda_\Sigma)$ closest to one. Despite the relatively large scatter in $\mathcal{S}(t)$, only a narrow range of λ_Σ can account for the observed amplitude. Contrary to Figs. 14 and 15, these data were not convolved by the beam.

Fig. 14.— Best match heavy disk model, with $\lambda_\Sigma = 4.93$ ($t = 2.85$ Gyr). *Left:* Synthetic column density map. *Center:* Synthetic velocity field. *Right:* Amplitude of the $m = 3$ component of the deprojected velocity field as a function of radius. The solid line represents the model ($V_3^{\rm sim}(r)$) and the dotted line the observations ($V_3^{\rm obs}(r)$). Convolution by a beam size of 45$''$ has been applied to the first two plots only.

Fig. 15.— Best match heavy disk model, with $\lambda_\Sigma = 4.93$ ($t = 2.85$ Gyr), in $(\log r, \theta)$ coordinates. The applied correction factor $q = 0.5$. Convolution by a beam size of 45$''$ has been applied.

Fig. 16.— Halo and disk circular velocity and cumulative mass profiles for our best match heavy disk model, with $\lambda_\Sigma = 4.93$ ($t = 2.85$ Gyr). *Left:* Scaled gas disk (*dotted line*), dark halo (*dashed line*), and total (*solid line*) circular velocity curves. *Right:* Disk (*solid line*) and halo (*dotted line*) cumulative mass profiles.

Fig. 17.— Surface density from our best match heavy disk model with $\lambda_\Sigma = 4.93$ (*solid line*), Kennicutt (1989) standard critical star formation threshold (*dashed line*), and our modified critical star formation threshold (*dotted line*). The observed velocity dispersion profile $\sigma_v(r)$ was used to derive all the curves.

Table 1. Bar masses for the runs presented in Figs. 8–10. The other bar parameters were kept fixed at $h_b = 3$ kpc, $b/a = 0.5$, and $n = 3$.

Ω_p (km s^{-1} kpc^{-1})	M_b (10^9 $M_\odot$)
5.0	4.9
5.5	5.7
6.0	6.8
6.5	5.1
7.0	4.8
7.5	4.7

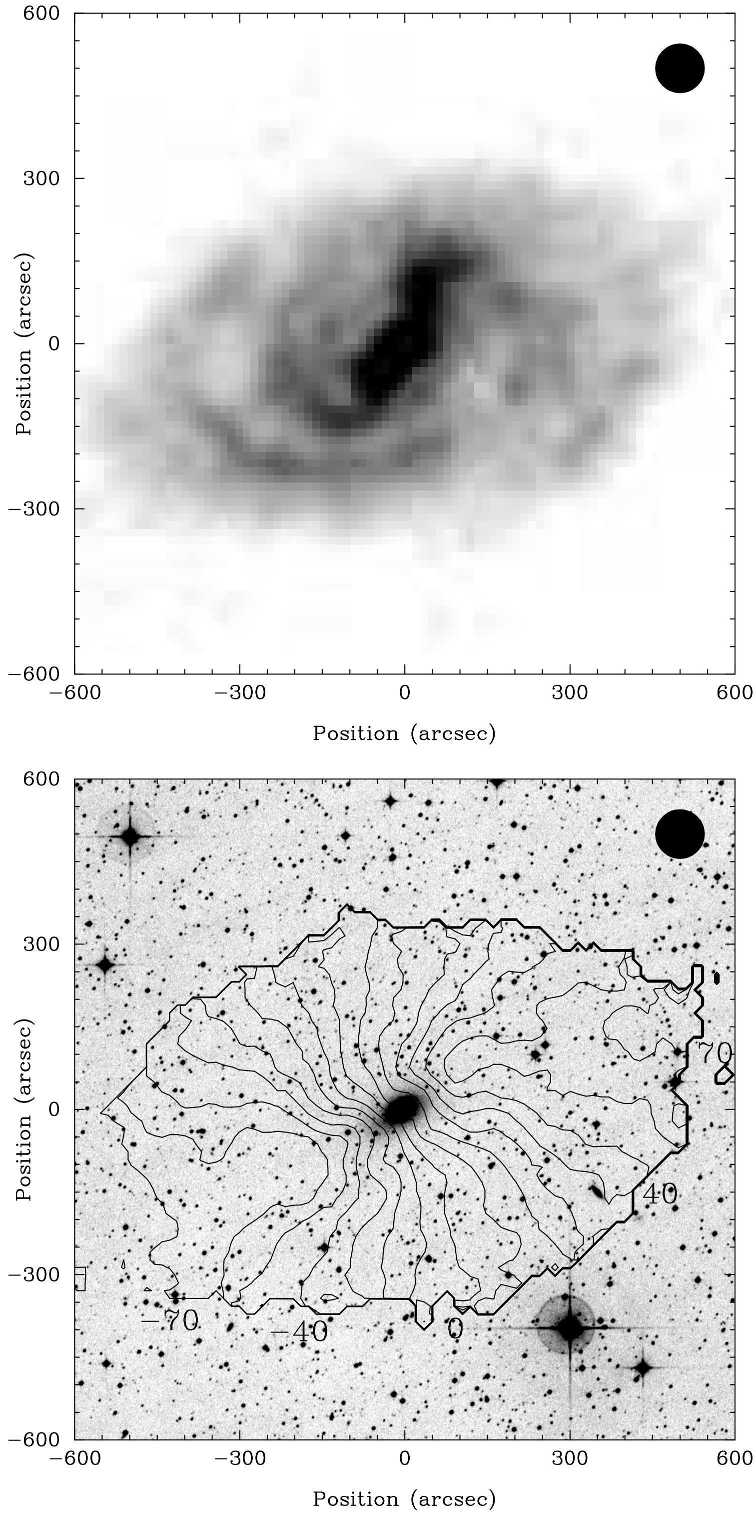
600
300
0
−300
−600
Position (arcsec)
−600
−300
0
300
600
Position (arcsec)
600
300
0
−300
−600
Position (arcsec)
70
40
−70
−40
0
−600
−300
0
300
600
Position (arcsec)

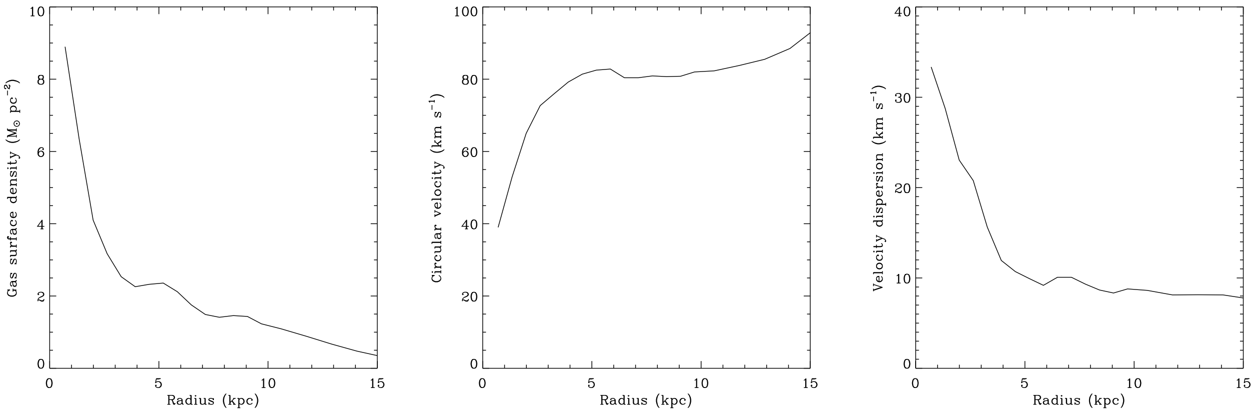
Gas surface density ($M_\odot$ pc^{-2})
Radius (kpc)
Circular velocity (km s^{-1})
Radius (kpc)
Velocity dispersion (km s^{-1})
Radius (kpc)

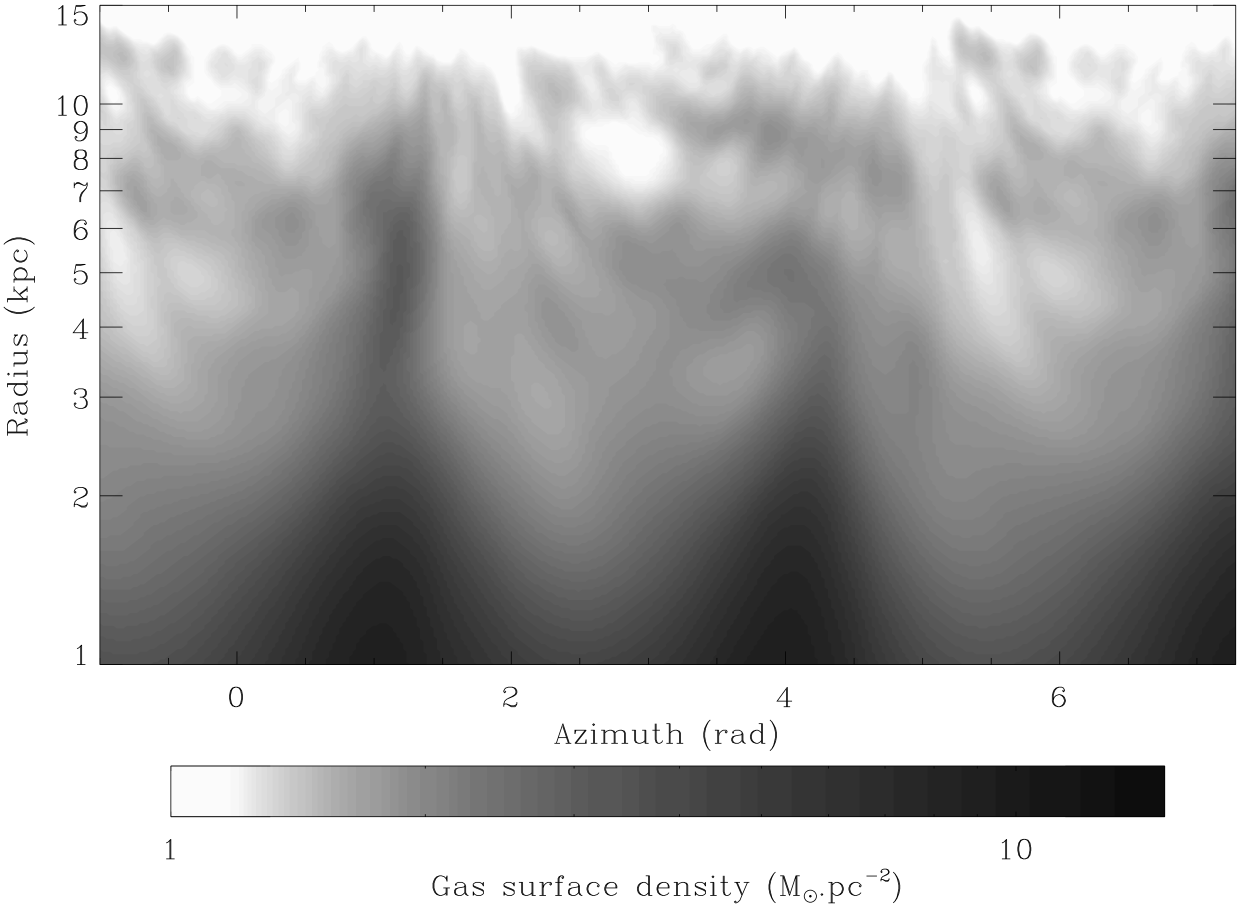
Radius (kpc)
15
10
9
8
7
6
5
4
3
2
1
0
2
4
6
Azimuth (rad)
1
10
Gas surface density ($M_\odot$.pc^{-2})

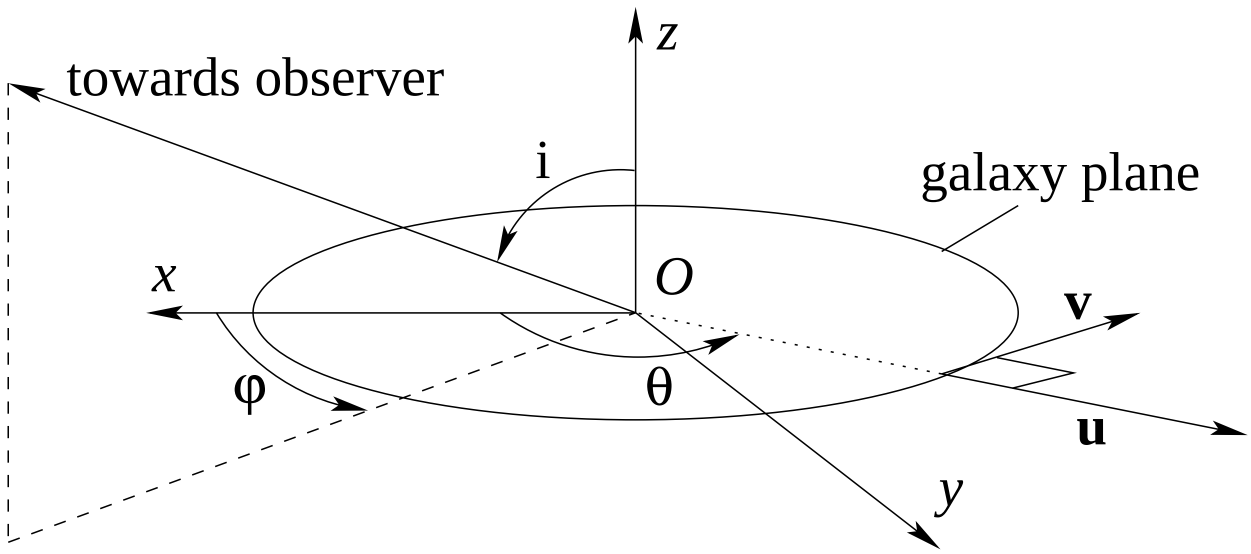
z
towards observer
i
galaxy plane
x
O
v
φ
θ
u
y

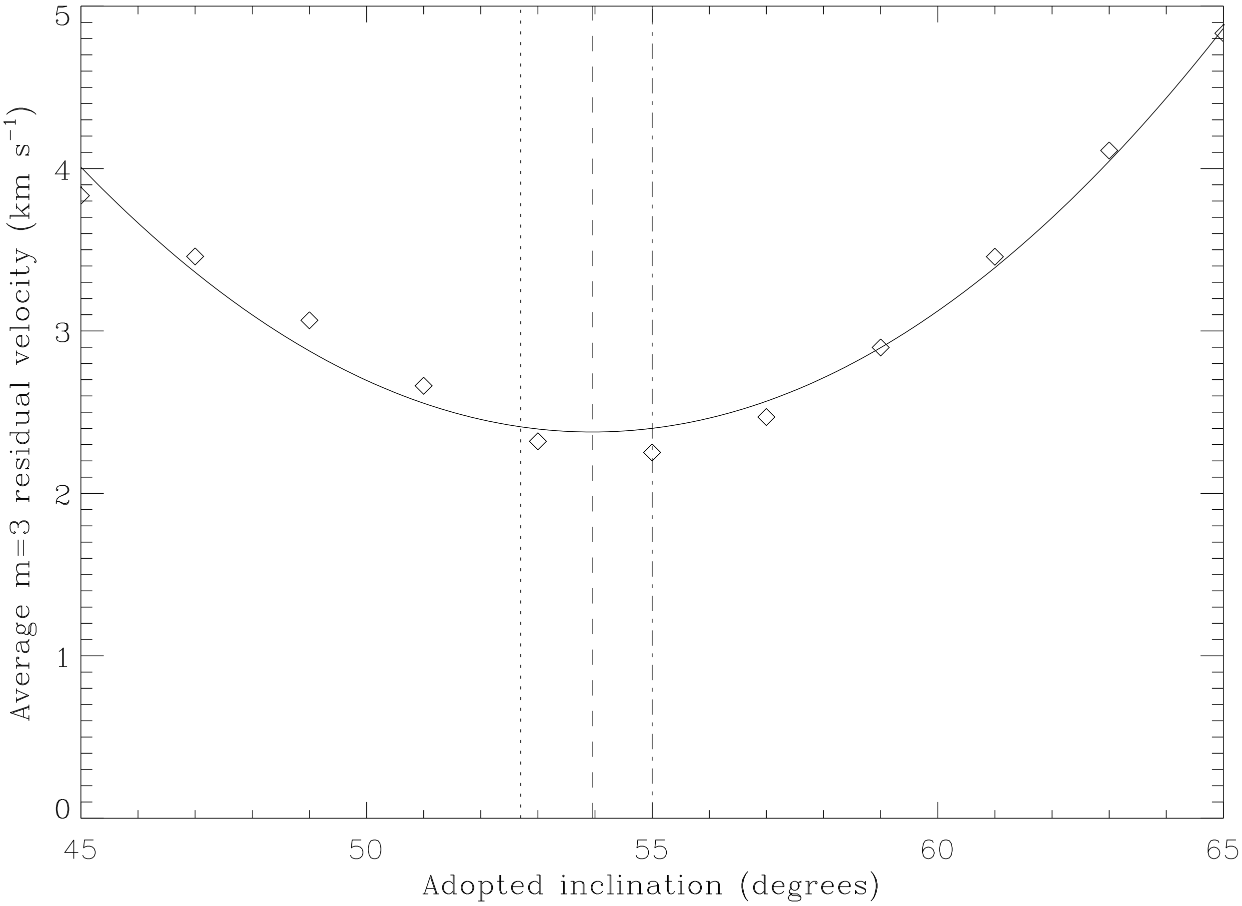
Average m=3 residual velocity (km s^{-1})
Adopted inclination (degrees)
0
1
2
3
4
5
45
50
55
60
65

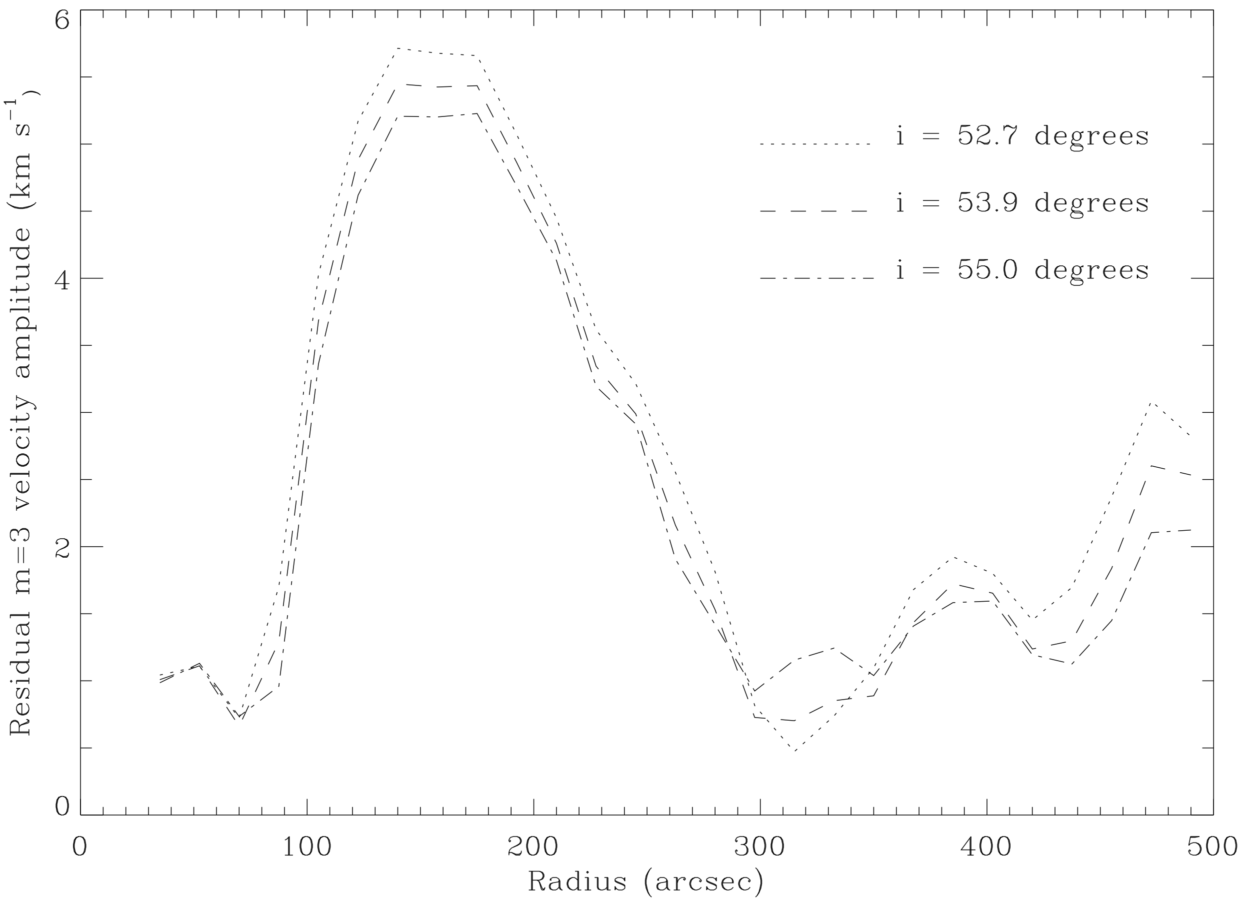
i = 52.7 degrees
i = 53.9 degrees
i = 55.0 degrees
Residual m=3 velocity amplitude (km s^{-1})
Radius (arcsec)
0
2
4
6
0
100
200
300
400
500

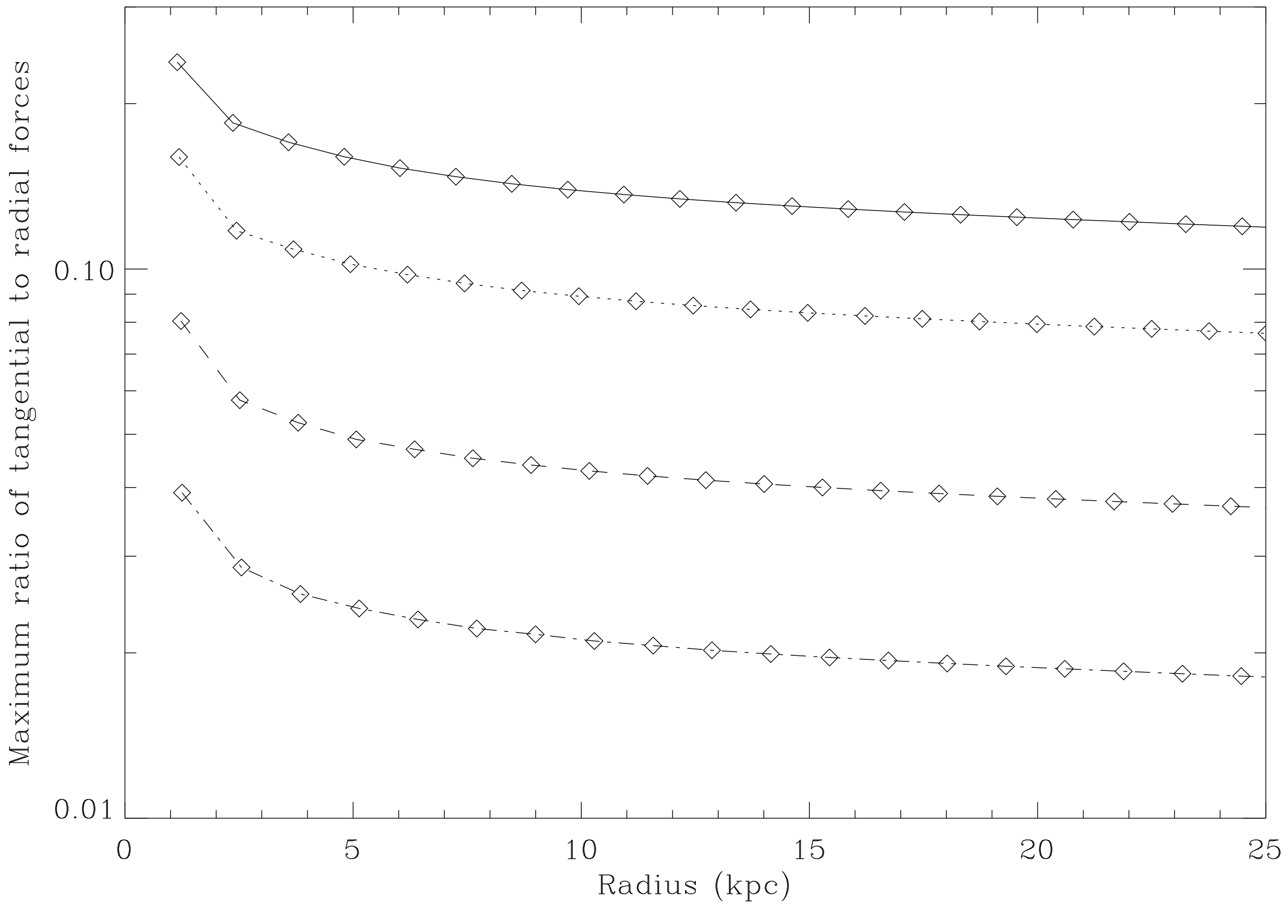

Maximum ratio of tangential to radial forces
0.10
0.01
0
5
10
15
20
25
Radius (kpc)

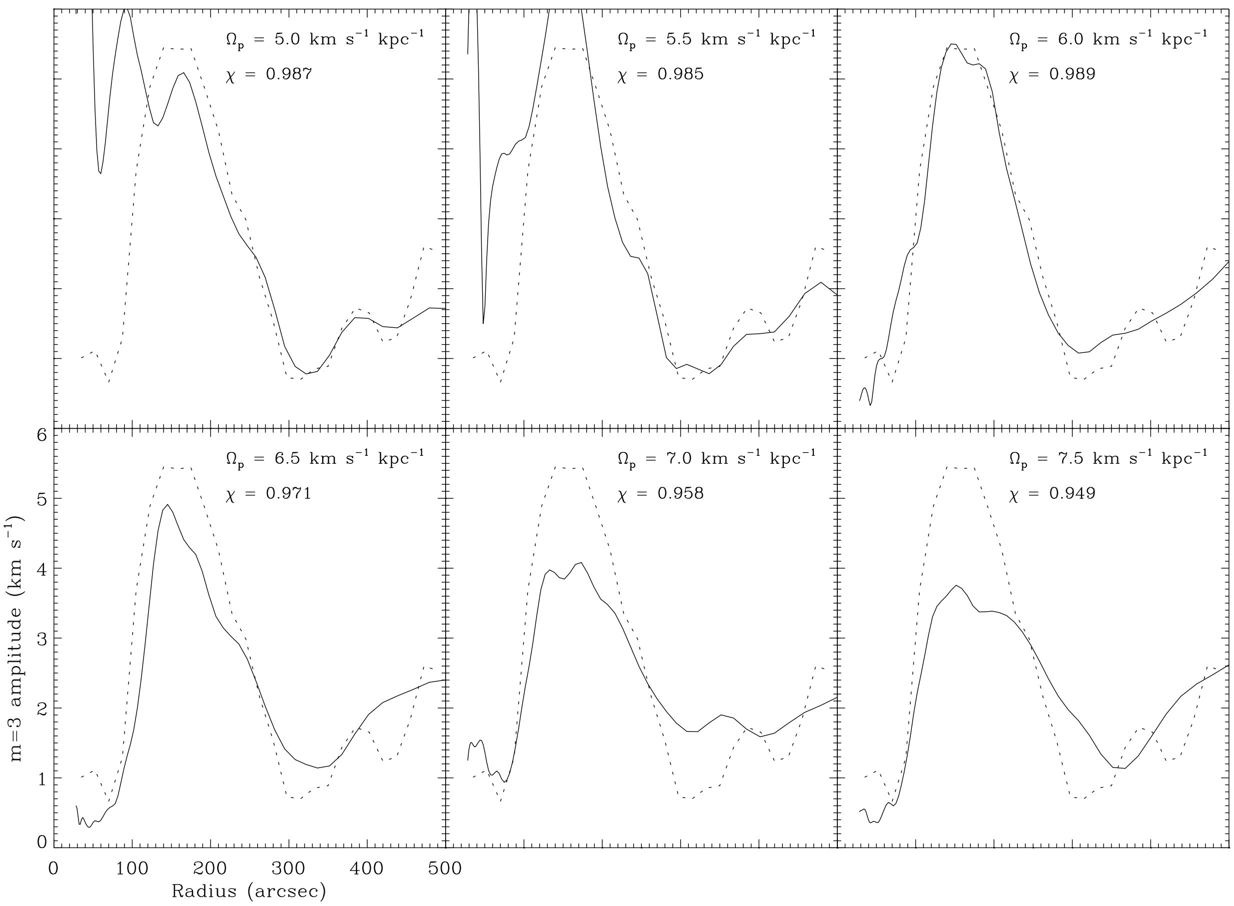

Ω_p = 5.0 km s^{-1} kpc^{-1}
χ = 0.987
Ω_p = 5.5 km s^{-1} kpc^{-1}
χ = 0.985
Ω_p = 6.0 km s^{-1} kpc^{-1}
χ = 0.989
Ω_p = 6.5 km s^{-1} kpc^{-1}
χ = 0.971
Ω_p = 7.0 km s^{-1} kpc^{-1}
χ = 0.958
Ω_p = 7.5 km s^{-1} kpc^{-1}
χ = 0.949
m=3 amplitude (km s^{-1})
0
1
2
3
4
5
6
0
100
200
300
400
500
Radius (arcsec)

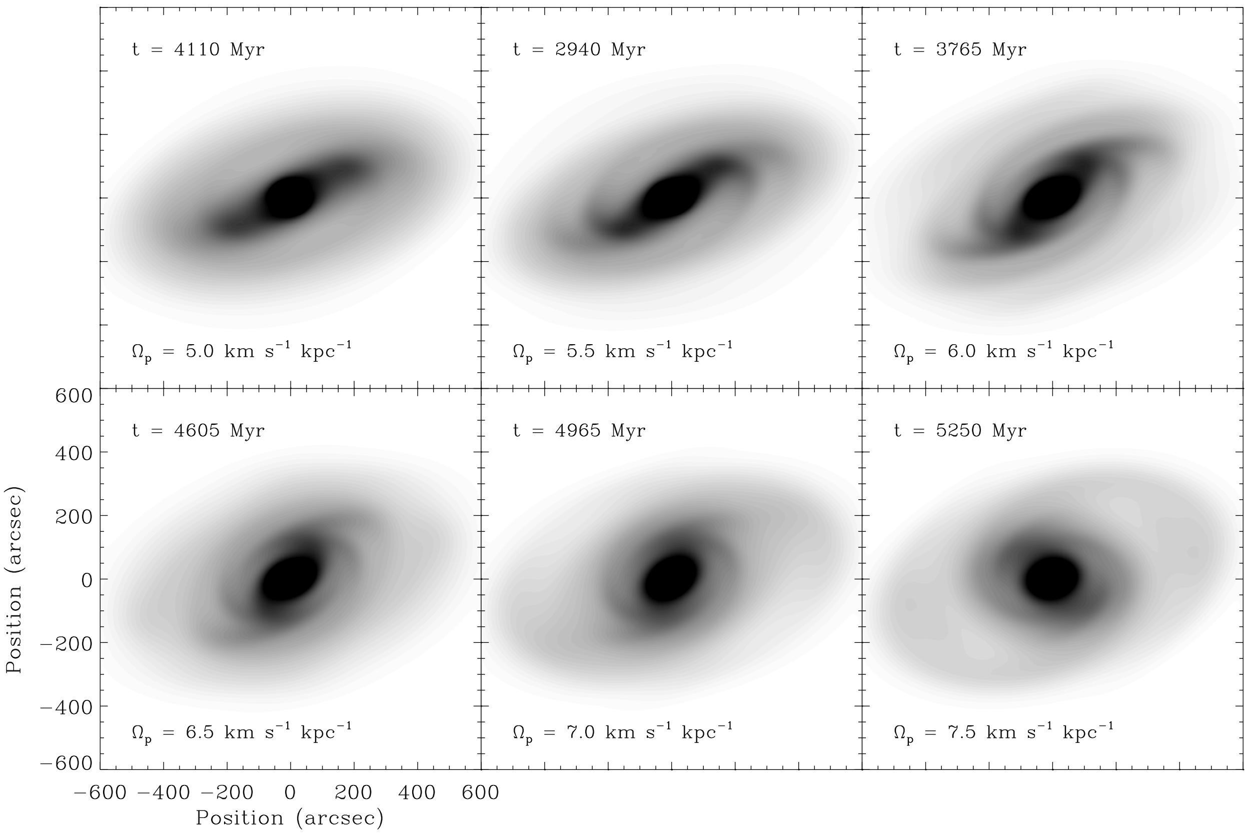

t = 4110 Myr
Ω_p = 5.0 km s^{-1} kpc^{-1}
t = 2940 Myr
Ω_p = 5.5 km s^{-1} kpc^{-1}
t = 3765 Myr
Ω_p = 6.0 km s^{-1} kpc^{-1}
t = 4605 Myr
Ω_p = 6.5 km s^{-1} kpc^{-1}
t = 4965 Myr
Ω_p = 7.0 km s^{-1} kpc^{-1}
t = 5250 Myr
Ω_p = 7.5 km s^{-1} kpc^{-1}
Position (arcsec)
600
400
200
0
−200
−400
−600
Position (arcsec)
−600 −400 −200 0 200 400 600

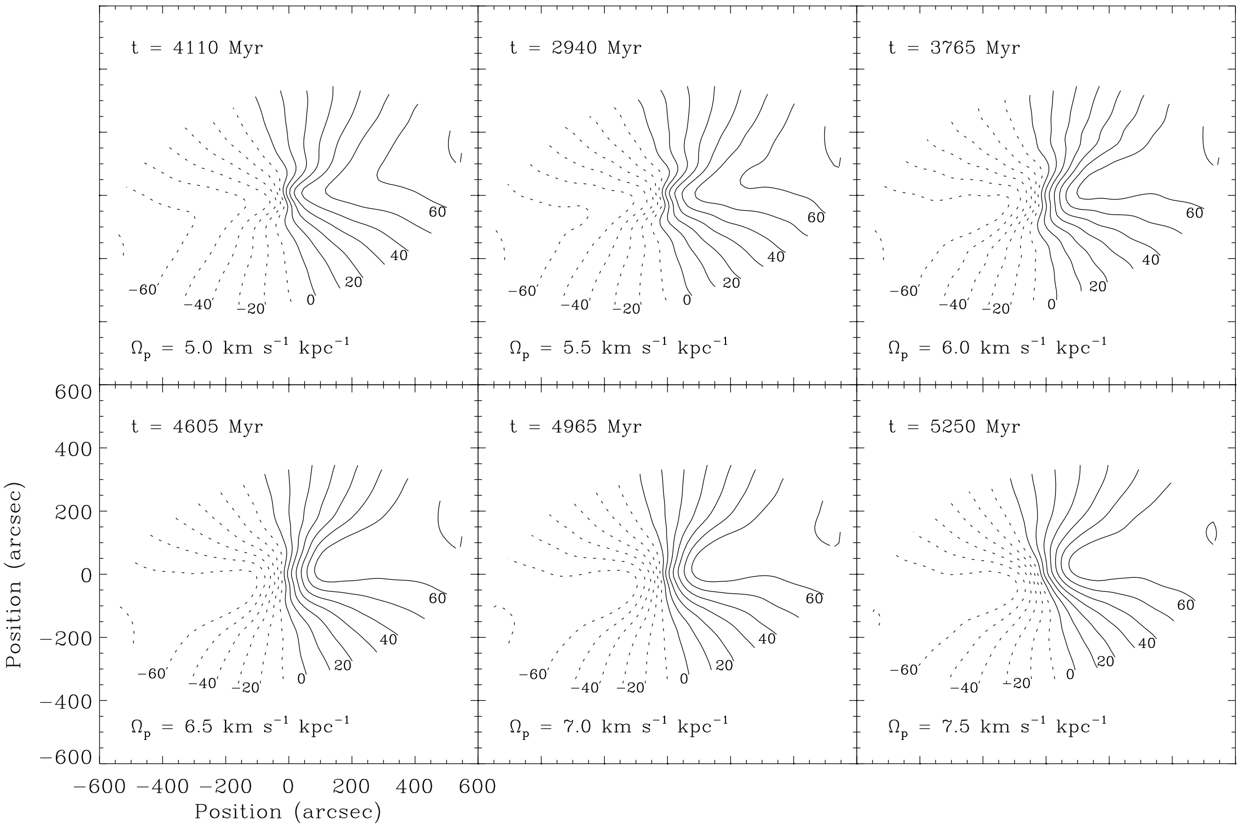
t = 4110 Myr
t = 2940 Myr
t = 3765 Myr
Ω_p = 5.0 km s^{-1} kpc^{-1}
Ω_p = 5.5 km s^{-1} kpc^{-1}
Ω_p = 6.0 km s^{-1} kpc^{-1}
t = 4605 Myr
t = 4965 Myr
t = 5250 Myr
Ω_p = 6.5 km s^{-1} kpc^{-1}
Ω_p = 7.0 km s^{-1} kpc^{-1}
Ω_p = 7.5 km s^{-1} kpc^{-1}
−60
−40
−20
0
20
40
60
Position (arcsec)
Position (arcsec)
−600 −400 −200 0 200 400 600
600 400 200 0 −200 −400 −600

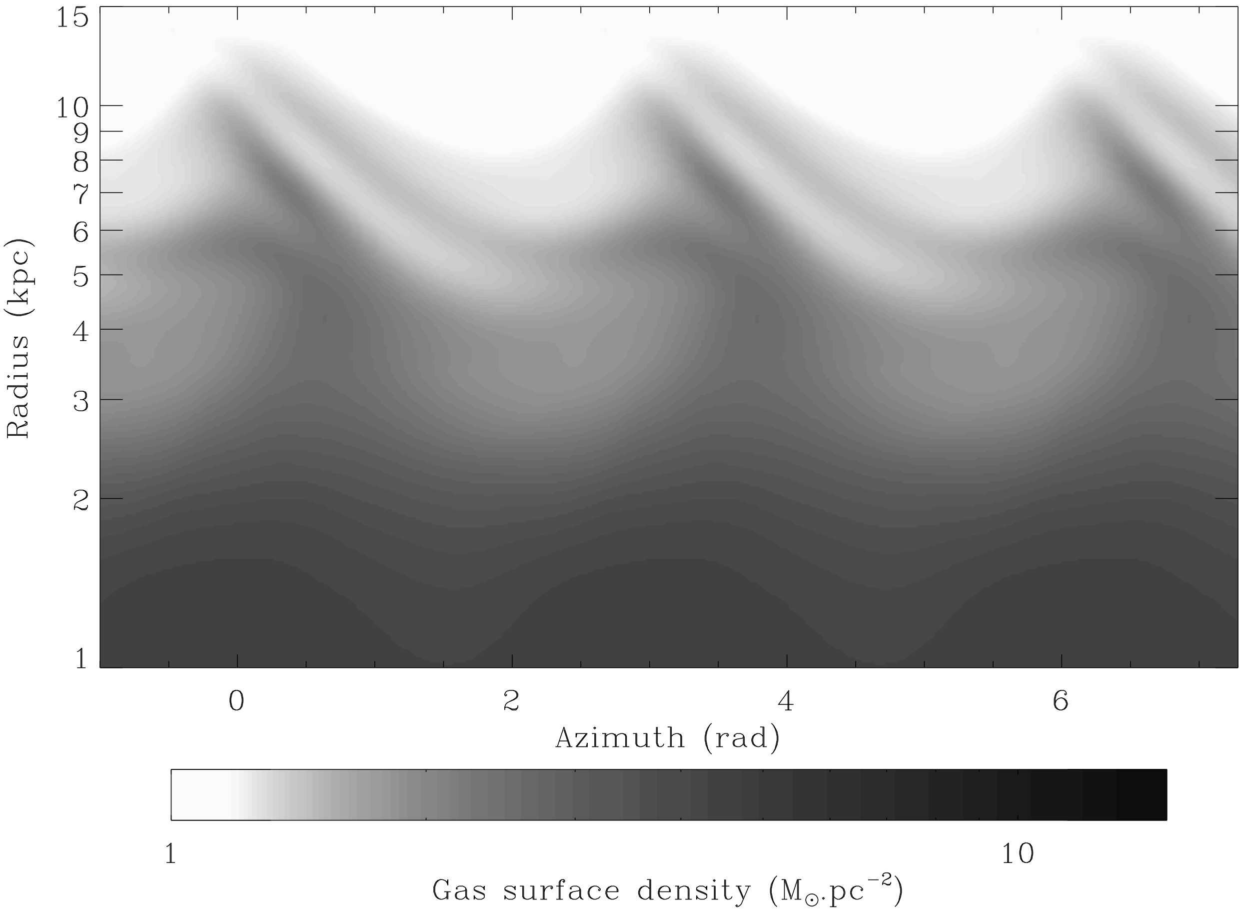

15
10
9
8
7
6
5
4
3
2
1
Radius (kpc)
0
2
4
6
Azimuth (rad)
1
10
Gas surface density (M$_\odot$.pc^{-2})

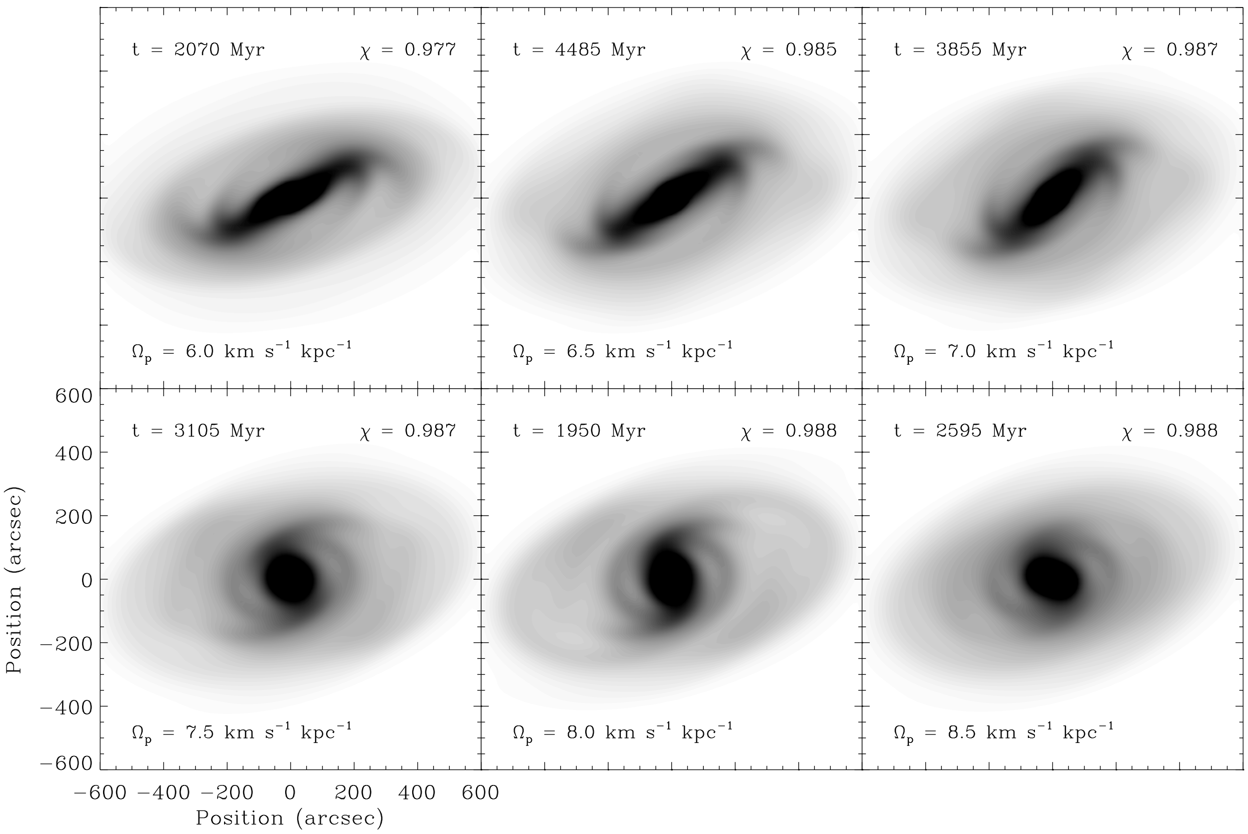
t = 2070 Myr
χ = 0.977
Ωp = 6.0 km s-1 kpc-1
t = 4485 Myr
χ = 0.985
Ωp = 6.5 km s-1 kpc-1
t = 3855 Myr
χ = 0.987
Ωp = 7.0 km s-1 kpc-1
t = 3105 Myr
χ = 0.987
Ωp = 7.5 km s-1 kpc-1
t = 1950 Myr
χ = 0.988
Ωp = 8.0 km s-1 kpc-1
t = 2595 Myr
χ = 0.988
Ωp = 8.5 km s-1 kpc-1
600
400
200
0
−200
−400
−600
Position (arcsec)
−600 −400 −200 0 200 400 600
Position (arcsec)

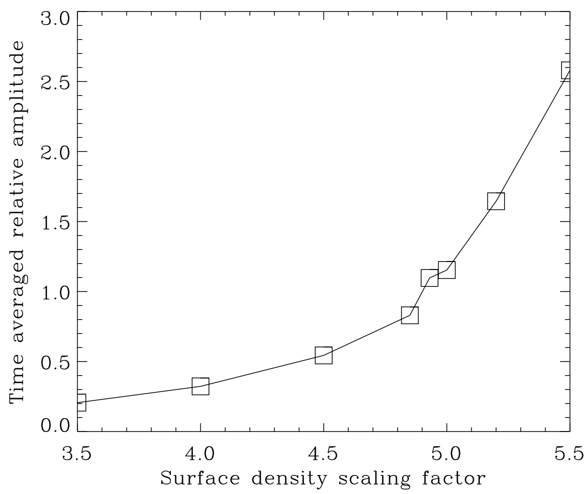

Time averaged relative amplitude
Surface density scaling factor
0.0
0.5
1.0
1.5
2.0
2.5
3.0
3.5
4.0
4.5
5.0
5.5

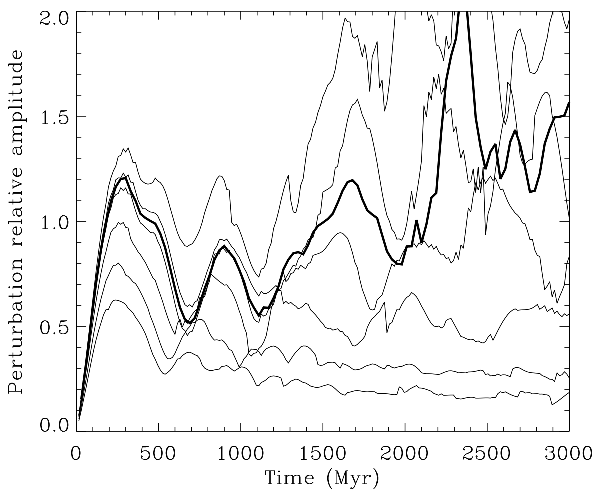

Perturbation relative amplitude
Time (Myr)
0.0
0.5
1.0
1.5
2.0
0
500
1000
1500
2000
2500
3000

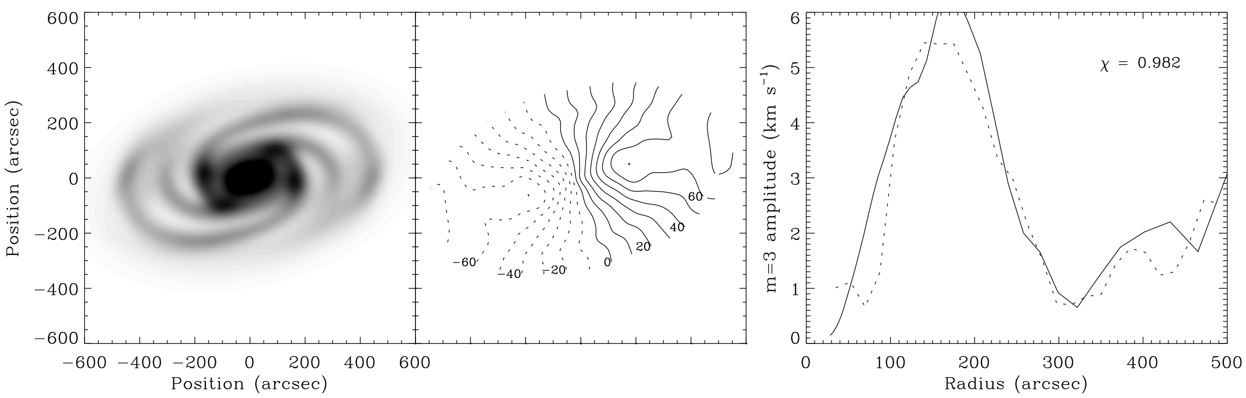
Position (arcsec)
Position (arcsec)
-60
-40
-20
0
20
40
60
m=3 amplitude (km s^{-1})
Radius (arcsec)
χ = 0.982

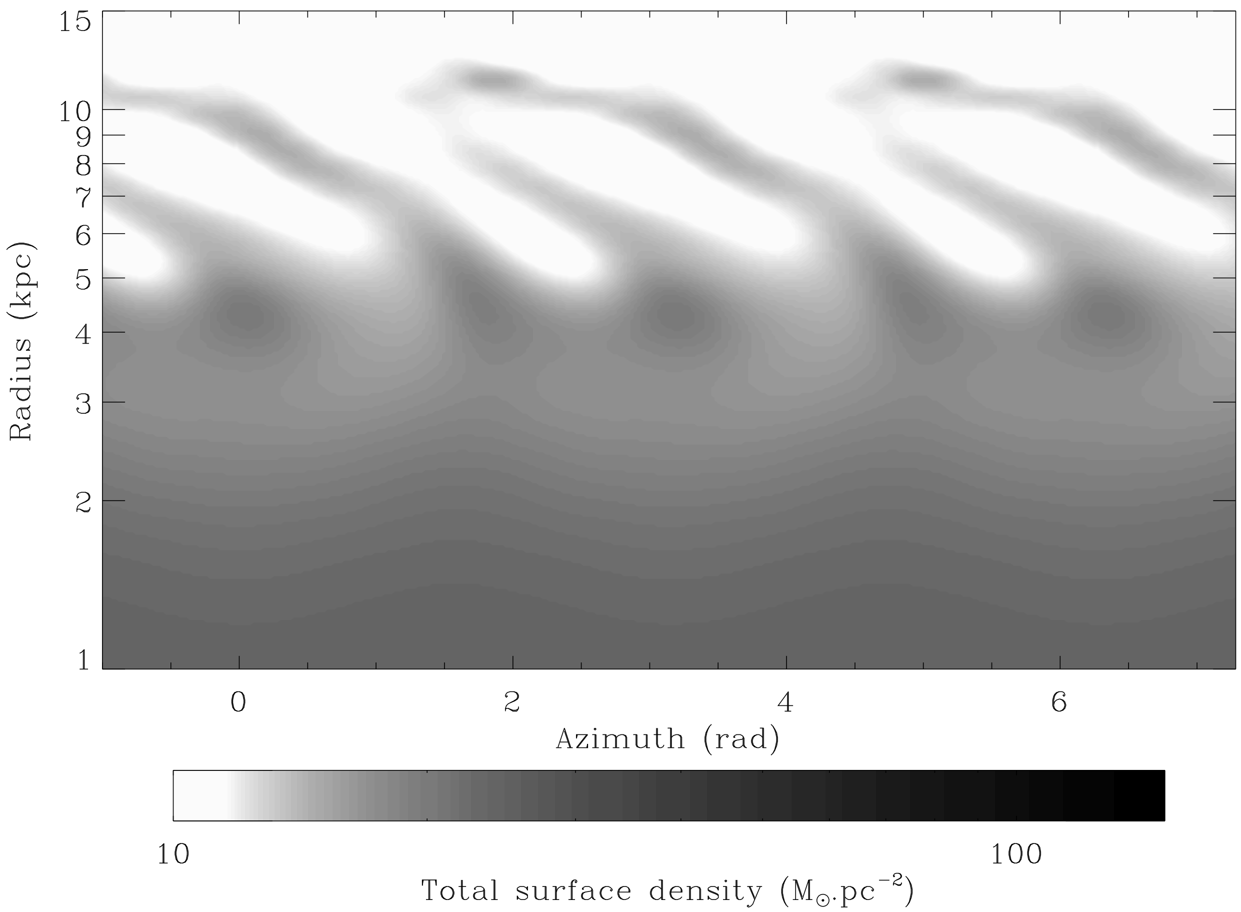
15
10
9
8
7
6
5
4
3
2
1
Radius (kpc)
0
2
4
6
Azimuth (rad)
10
100
Total surface density (M$_\odot$.pc^{-2})

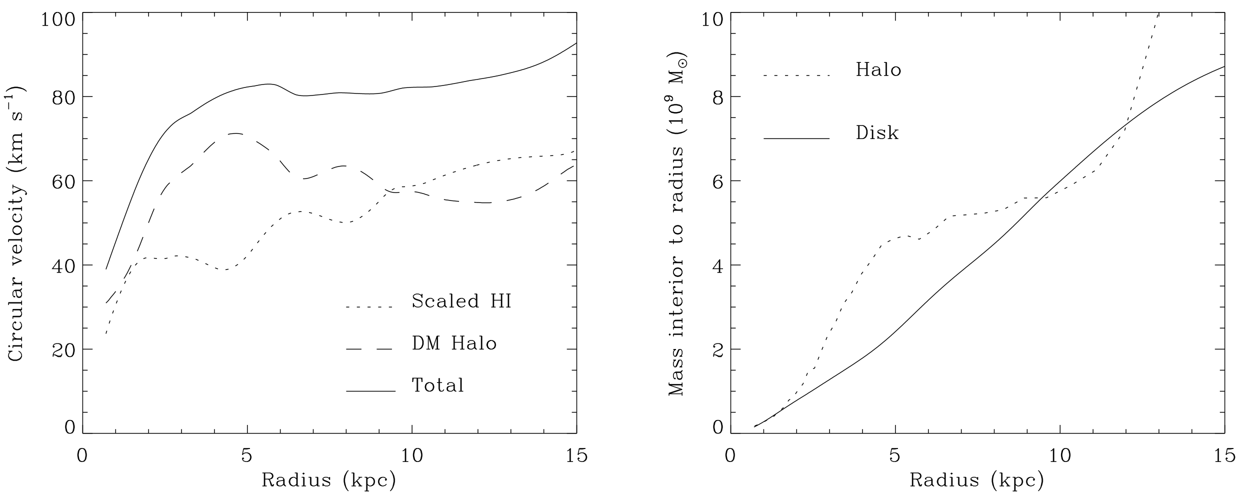

Circular velocity (km s^{-1})
Radius (kpc)
Scaled HI
DM Halo
Total
Mass interior to radius (10^9 M$_\odot$)
Radius (kpc)
Halo
Disk

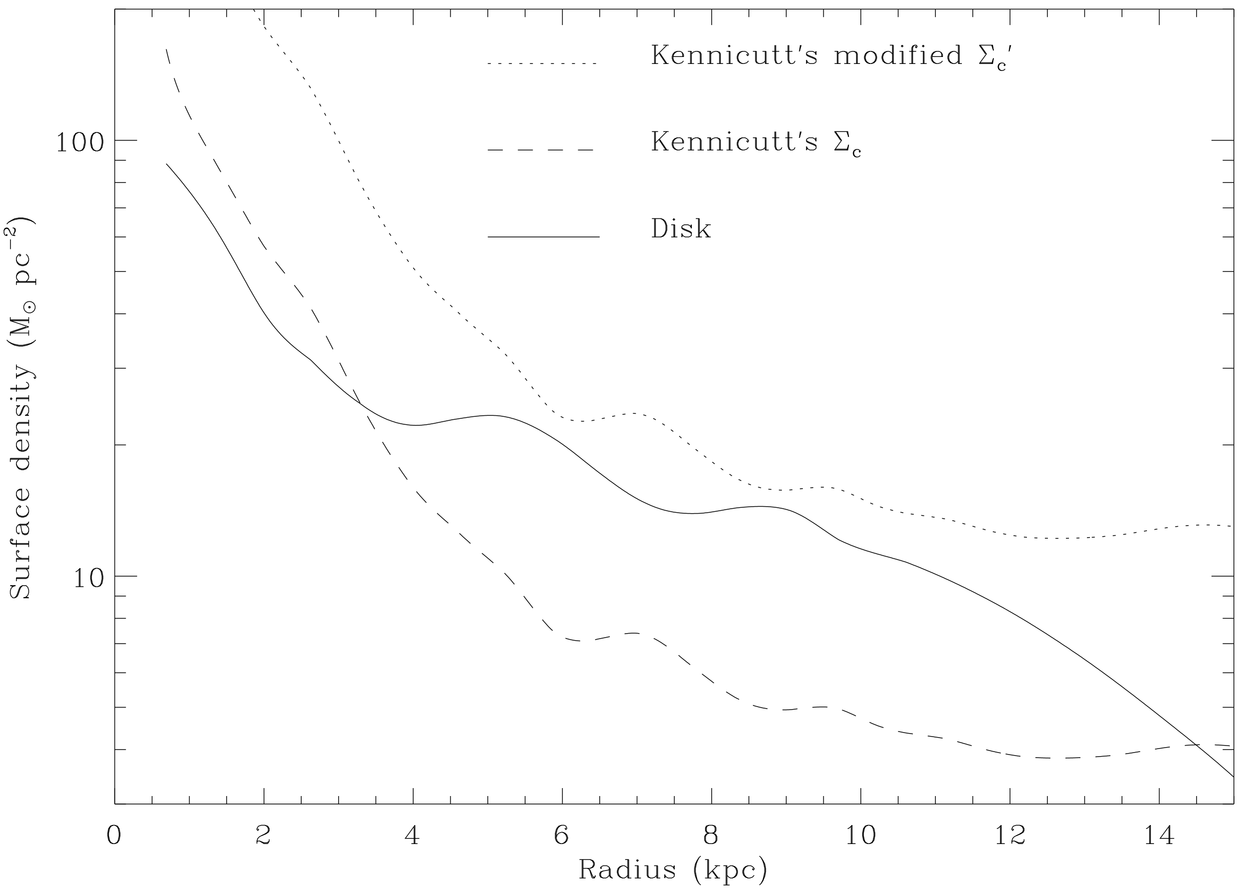
Kennicutt's modified Σ_c'
Kennicutt's Σ_c
Disk
Surface density ($M_\odot$ pc^{-2})
100
10
0
2
4
6
8
10
12
14
Radius (kpc)